Preprint — Accepted for publication in *Bulletin of Volcanology*
Citation: Fee, D., Tan, D., Haney, M., Merritt, K., Lyons, J., Wech, A., Loewen, M., Boyce, E. S., and Scamfer, L. (in press). Seismic and infrasound signals from the 2023 explosive eruption sequence of Shishaldin Volcano, Alaska. Bulletin of Volcanology. https://doi.org/10.1007/s00445-026-01951-3

Seismic and infrasound signals from the 2023 explosive eruption sequence of Shishaldin Volcano, Alaska

David Fee[1*], Darren Tan[1], Matthew Haney[2], Karenna Merritt[1], John Lyons[2], Aaron Wech[2], Matthew Loewen[2], Eleanor Boyce[1], Logan Scamfer[1]

[1*]Alaska Volcano Observatory, Geophysical Institute, University of Alaska Fairbanks, 2156 Koyukuk Dr, Fairbanks, 99775, AK, USA.
[2]U.S. Geological Survey, Alaska Volcano Observatory, 4230 University Drive, Anchorage, 999508, AK, USA.

*Corresponding author(s). E-mail(s): dfee1@alaska.edu;
Contributing authors: ptan@alaska.edu; mhaney@usgs.gov; kamerritt@alaska.edu; jlyons@usgs.gov; awech@usgs.gov; mloewen@usgs.gov; esboyce@alaska.edu; ltscamfer@alaska.edu;

Abstract

Shishaldin Volcano, Alaska erupted in 2023 with 13 explosive paroxysms over a 4 month period, producing notable seismic and low frequency acoustic (infrasound) signals recorded on a local geophysical network. We describe the pre-, syn-, and post-eruptive seismoacoustic signals from the 2023 eruption sequence. Using a recently developed machine learning classifier, we detect and categorize diverse seismicity, including sustained precursory tremor that began months before the first eruption. Explosive events exhibit similar repose periods and relatively consistent high-amplitude, broadband seismic tremor, building over hours to days and at times enabling short-term eruption forecasts. In contrast, co-eruptive infrasound consists of complex mixtures of weak to energetic discrete events and continuous tremor or jetting. The infrasound characteristics suggest that the paroxysmal phase of some eruptions was driven by discrete, energetic Strombolian explosions rather than sustained fountaining, highlighting variability among basaltic explosive styles. The seismoacoustic observations align with a foam-reservoir mechanism, where deep gas flux formed a foam that collapsed periodically to drive eruptions, while a late-stage shallow intrusion increased leakage

and continuous degassing and seismicity. These results have important implications for eruption forecasting and hazard monitoring and demonstrate the utility of combining seismic and infrasound data to understand eruption dynamics.

Keywords: Shishaldin, seismic, infrasound, explosive eruption

1 Introduction

Shishaldin Volcano is one of the most active volcanoes in the Aleutian Arc. This remote volcano located on Unimak Island is notable for its frequent eruptions, conical shape, and often explosive basaltic eruptions. A series of eruptions in 1999 produced significant ash plumes and debris flows that have been studied in detail through geophysical (Vergniolle et al. 2004; Thompson et al. 2002; Caplan-Auerbach and McNutt 2003; Vergniolle and Caplan-Auerbach 2006), remote sensing (Nye et al. 2002; Dehn et al. 2002), and geochemical (Nye et al. 2002; Stelling et al. 2002; Rasmussen et al. 2018) analyses. Low-level eruptions occurred in 2004 and 2014, followed by an eruption in late 2019 and early 2020 (Angarita et al. this issue; Orr et al. 2023) that produced three paroxysms with ash plumes up to 9.8 km above sea level (ASL) and fed a lava flow (Loewen this issue; Gomez-Patron et al. this issue). After an approximately three-year period of quiescence, Shishaldin erupted explosively on July 14, 2023. Twelve additional explosive events followed over the next four months. These explosive events contained relatively similar inter-eruptive durations (repose periods) for many events (Loewen this issue), significantly eroded the summit region (Angarita et al. this issue; Waythomas this issue), and had increases in seismic and low frequency acoustic (infrasound) tremor amplitudes prior to and during each eruption. All 13 eruptions produced considerable ash and gas (detected as SO_2) plumes, with heights up to 14 km ASL (Gomez-Patron et al. this issue; Lopez et al. this issue) and extensive pyroclastic density currents and lahars generated on the volcano's flanks (Waythomas this issue). Volcanic lightning was detected for multiple events (Mota this issue). The paroxysmal phase of at least two events produced gravity waves detected on nearby seismic and infrasound stations (Haney et al. this issue). The at-times regular event repose time and seismic tremor build-up during the explosive events allowed the Alaska Volcano Observatory (AVO) to forecast some of the eruptions. Newly developed data assimilation techniques used the seismic data to quantitatively hindcast the paroxysmal phase of some events (Girona et al. this issue).

AVO monitors Shishaldin with a combination of ground and satellite-based sensors. Three geophysical stations with colocated seismic, infrasound, and Global Navigation Satellite System (GNSS) sensors form the backbone of the monitoring network (Fig. 1a), along with tilt and webcam data. The seismoacoustic signals from the 1999 eruptions have been studied in detail, and they have provided valuable information on both the subsurface processes (e.g., Caplan-Auerbach and McNutt 2003) and eruption dynamics (e.g., Vergniolle 2024). The geophysical signals from the 2023 eruption have a number of similarities to the 1999 eruption, but perhaps more interesting are their differences. In particular we highlight the relatively high number of explosive events

and similar seismic amplitude trends between events. These trends resemble those from Mt. Etna, Italy (Andronico et al. 2021; Sciotto et al. 2019), which is a frequently erupting basaltic volcano and considered an analog for Shishaldin both geologically (Stelling et al. 2002) and in terms of eruption style (Vergniolle et al. 2004).

Shishaldin magmas have a relatively low silica content for a volcanic arc stratovolcano, with both the 1999 and 2023 eruptions having clear basaltic compositions with SiO_2 content of 48-50% (Izbekov et al. this issue; Stelling et al. 2002; Rasmussen et al. 2018). Such low viscosity magmas have been proposed to facilitate two phase flow (gas and magma) during eruptions, which has important implications for eruption dynamics and associated hazards (e.g., Houghton and Gonnermann 2008). Other basaltic stratovolcanoes show similar explosive eruption styles to Shishaldin. Paroxysms at Etna (Andronico et al. 2021; Ulivieri et al. 2013), Fuego (Lyons et al. 2025), and Villarica (Romero et al. 2018) often have a gradual transition from Strombolian explosions to vigorous fountaining and occasionally high tephra columns. Building off work at these volcanoes with similar eruption styles and magma composition, the seismoacoustic signals from Shishaldin can provide unique insight into the two phase flow dynamics and eruption processes. In particular, we contend the infrasound signals can be used to determine changes from slug to churn-annular flow (Ulivieri et al. 2013; Spina et al. 2019), which has implications for the subsequent plumes and hazards.

Here we present an overview of the seismoacoustic signals from the 2023 Shishaldin eruption. First we describe the local monitoring network and available data in Section 2.1. In Section 2.2 we describe the various methods we use to detect and characterize the seismic and infrasound signals, with the results then detailed in Section 3. Section 4 compares the 2023 eruption signals to past events and discusses potential seismoacoustic and eruption source models.

2 Data and Methods

2.1 Data

Shishaldin is monitored by a 3-station geophysical network with stations at approximately 5–10 km distance from the summit vent (Fig. 1). Stations SSLS, SSLN, and SSBA have colocated seismic and infrasound sensors. Three component seismic data are recorded using Nanometrics Trillium Compact Posthole sensors with a 120 s low corner. The seismometer at SSLN was misoriented 180 °during this period, which is reflected in the BHN and BHE channel metadata. Infrasound data are recorded using Chaparral Physics Model 64 UHP-2 sensors with a flat response between 0.02–200 Hz. The seismoacoustic data are digitized using Nanometrics Centaur digitizers at 50 Hz and are transmitted in real-time to AVO. Infrasound data are ported to the atmosphere at each instrument enclosure with no noise reduction systems installed, and are offset from the seismometer by a few meters. Nearby stations ISNN, ISLZ, BRPK, and WTUG at distances of 15–29 km from the vent also have Nanometrics Trillium Compact Posthole seismometers, and BRPK, ISLZ, and WTUG have webcams. The infrasound sensor at station SSBA had an abnormal, non-physical response in 2023, and we do not analyze those data here and suggest it be generally disregarded for 2023 eruption analysis.

Data outages occurred on the Shishaldin network in 2023 due to a combination of severe weather, deep snow, possible bear damage, and intermittent radio network issues. Figure 1b shows the 1 hr data availability for the local seismoacoustic network surrounding the eruption. The explosive events are numbered and marked by red dashed lines. SSLS had regular real-time transmission-related outages during the eruption, but missing data were also stored locally and back-filled after site visits in 2023 and 2024, allowing a nearly complete record of the eruption sequence (Fig. 1d). SSBA recorded the first half of the eruption well and was relied on by AVO for seismic monitoring, but then had power issues starting in mid-September and recorded data intermittently for the rest of the eruption (Fig. 1c). SSLN was not recording data in the first half of 2023 due to power issues that were resolved by a site visit in late August 2023, and then it recorded Events 9–13 with generally high signal-noise ratio (SNR) (Fig. 1b). Overall SSLS has the most complete and high-quality recordings of the eruption in both the seismic and infrasound data and we focus on those data here.

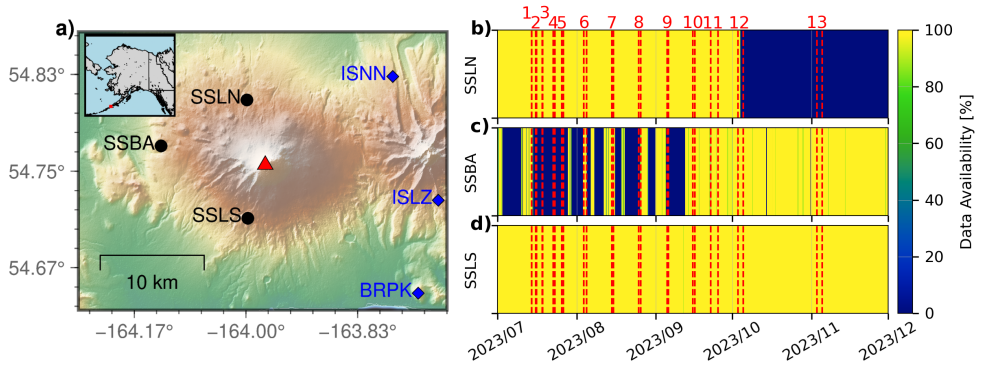

Fig. 1 Shishaldin seismoacoustic network map and data availability. a) Map of seismoacoustic stations surrounding Shishaldin, including an inset showing the Alaska region and red box for the study area. Three stations (SSLS, SSLN, and SSBA) have colocated seismic and infrasound sensors and are noted by black circles, and they are 5.5, 6.4, and 10.2 km from the vent, respectively. SSBA is located ≈50 m from a previous station named SSLW. Nearby seismic stations are shown as blue diamonds. Shishaldin's summit is marked by a red triangle. b–d) Hourly data availability for SSLS, SSBA, and SSLN between July 1–December 1, 2023. The explosive events are numbered and marked by red dashed lines.

2.2 Methods

We utilize a recently developed machine learning model to detect and classify the seismicity surrounding the 2023 Shishaldin eruption. Our aim is to create an objective, quantitative catalog of seismicity both for the entire eruption sequence and as a comparison between individual explosive events. Tan et al. (2024) constructed the

VOlcano Infrasound and Seismic Spectrogram Network (VOISS-Net) using a Convolutional Neural Network to classify 4 min spectrograms into six volcano seismicity and four infrasound classes for Pavlof Volcano, Alaska. Their primary goal was to provide a continuous classification of the volcanic tremor at Pavlof. Lyons et al. (2025) then added a Long Period (LP) seismic event class to VOISS-Net and applied it to 5 years of seismic data at Semisopochnoi Volcano, Alaska. Fee et al. (2025) then generalized the Tan et al. (2024) VOISS-Net model to detect and classify volcano seismicity at any volcano globally. Notable changes by Fee et al. (2025) to the original model are a switch to 2 minute spectrograms, labels from 7 additional volcanoes, and an additional LP class. This model achieved an accuracy of 87% on its test set. Here we use the generalized VOISS-Net model of Fee et al. (2025) to systematically detect and classify the seismicity at Shishaldin surrounding the 2023 eruption into seven classes: Broadband Tremor, Harmonic Tremor, Monochromatic Tremor, Explosions, Earthquakes, LPs, and Noise. The seismic data from the available three local stations are used, although data from some stations are not available at times due to station outages (Fig. 1b–d). VOISS-Net classifies the spectrograms for each station and returns a classification probability from 0–1, followed by a final "network vote" combining the probabilities from each station to reduce outliers and station disagreement. A network probability, termed P_{norm}, is utilized to remove poor classifications, and we set a P_{norm} threshold of 0.4. VOISS-Net is applied to 2 min spectrograms with 50% overlap, and the spectrograms are constructed using 10 s Hann windows and 90% overlap.

Seismic and infrasound amplitudes are analyzed by computing Reduced Displacement (D_R) and Root-Mean-Squared pressure (RMS_p), respectively. Reduced Displacement is a commonly used volcano seismic metric that normalizes the amplitudes by correcting for instrument response and geometric spreading (Aki and Koyanagi 1981; Fehler 1983). It is a useful metric as it permits comparison of seismic amplitudes between different seismic stations, volcanoes, and eruptions. D_R for body waves is computed by taking the RMS seismic displacement (u) and multiplying by the source-receiver distance:

$$D_R = u_{\mathrm{RMS}} \times r \tag{1}$$

The geometric spreading factor is assumed to be spherical for body waves. Here we assume the seismic wavefield from Shishaldin in our frequency band of interest is primarily composed of surface waves (Thompson et al. 2002) and follow Fehler (1983) to account for cylindrical spreading of surface waves:

$$D_R = u_{\mathrm{RMS}} \times \sqrt{\lambda r} \tag{2}$$

where λ is the surface wave wavelength. We assume a dominant frequency of 2 Hz and velocity of 1500 m/s for a wavelength of 750 m. D_R is then multiplied by 10,000 to convert to cm^2. D_R calculations are made by using a running median over 5 min data segments with 80% overlap between 1–10 Hz, the dominant tremor band. For a source location, we assume a straight line distance from each station to Shishaldin for distances of 5.468, 6.431, and 10.230 km for SSLS, SSLN, and SSBA, respectively.

We compute D_R for each station (SSLS, SSLN, and SSBA) but use SSLS as the primary station for analysis since it has the most complete record and is the closest

to the volcano (Fig. 1a). Most past studies of Shishaldin used short-period, analogue station SSLW for D_R computation (Thompson et al. 2002; Caplan-Auerbach and McNutt 2003). The digital, broadband station SSBA was installed nearby SSLW in 2008, with the stations offset by ≈50 m (Fig. 1a), therefore we assume SSBA D_R values are comparable to SSLW. We calculate a scaling factor for SSLS and SSLN relative to SSBA for historical comparison and consistency. Figure 2 shows the running D_R values for SSBA, SSLN, and SSLS for a 12 hr period encompassing 2023 Event 12. We calculate the median D_R ratio by dividing SSLN and SSLS by SSBA values to get scaling factors of 3.63 and 2.02, respectively (dashed lines in Fig. 2d). All SSLS D_R values shown hereafter are computed using the 2.02 scaling factor. This scaling is also performed in Loewen (this issue). The D_R variability between stations is most likely related to either path or site effects that we are not able to resolve. We computed D_R scaling factors for other events when multiple stations were operating and found similar values. All times listed are in UTC and all plume heights are in height ASL and taken from Loewen (this issue) and Gomez-Patron et al. (this issue).

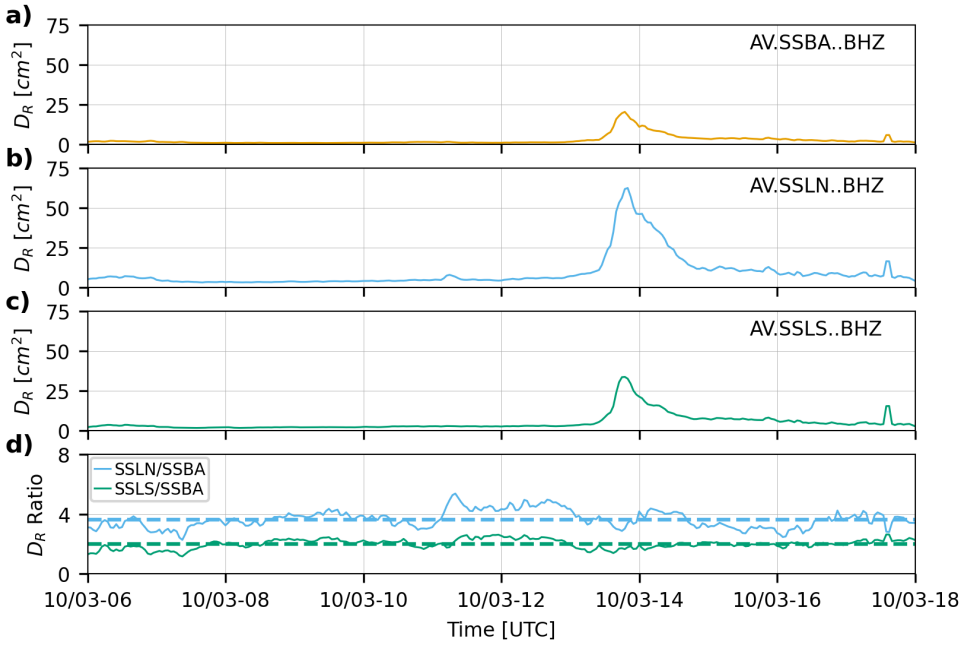

Fig. 2 Example of D_R variability and scaling among stations for Event 12, which occurred on October 3, 2023. a)–c) D_R is computed for each station for 12 hr. d) The D_R ratio between stations SSLN (blue) and SSLS (green) relative to SSBA (orange) is plotted as a solid line, with the median value plotted as a dashed line.

Infrasound amplitudes are analyzed by computing the RMS pressure (RMS_p) on SSLS. We first filter the data between 0.5–10 Hz which is where the infrasound signals are focused. RMS_p is then computed in 5 min segments with 50% overlap. RMS_p is not comparable between stations as it does not account for acoustic propagation from the source to receiver, which is beyond the scope of this work. Numerical simulations (e.g., Kim et al. 2015) and/or high-resolution atmospheric models (e.g., Johnson et al. 2012) would be needed to accurately model the acoustic wave propagation. We do assume RMS_p is comparable between explosive events in 2023 at SSLS but acknowledge that some changes in the source and propagation affect the relative amplitudes. Unless otherwise noted, spectrograms for the seismic and infrasound data are computed using the Welch periodogram with 100 s segments with 50% overlap. Spectrogram amplitudes are converted to dB using a reference of 1 m/s and 20 μPa for the seismic and infrasound, respectively.

Seismic and infrasound start and end times are determined manually and are detailed in Tables 1 and 2. Eruption seismicity is determined based on deviations above and then a return to background on the D_R timeseries in conjunction with the presence of broadband tremor (both visually and via VOISS-Net). We attempted to use automated methods, such as the appearance of sustained broadband tremor via VOISS-Net, to determine the event seismic start and end times, but found this unreliable due to the wide variety of seismicity present before and after each event. Subtle seismic tremor and LP events exist before and after our derived start and end times, sometimes for days to weeks. Infrasound start and end times are also determined based on a combination of visual analysis of the RMS_p and spectrograms. Eruption signals generally demonstrate clear discrete events, spectral peaks, diffuse harmonics, or a gradual ramp-up and decay, whereas wind noise is characterized by abrupt temporal changes and a characteristic linear decay with frequency. Two co-authors independently performed a blind analysis of these two infrasound products, and subsequently compared and combined their results. Wind noise often masks the infrasound signals, and thus complicates fully accurate start and end times. Note no infrasound signals are unambiguously identifiable in the local infrasound data for Events 7 and 9. Regional infrasound arrays also detected infrasound signals from both explosive and background activity in 2023, but are not discussed here due to the generally higher SNR on the local stations and greater infrasound propagation issues at longer ranges. D_R, RMS_P, and seismic and infrasound start and end times are available and described in context of the eruption sequence in Loewen (this issue). We note that eruption start and end times are poorly constrained by the very limited number of clear webcam images.

We analyze acoustic-seismic coupling and contamination using the recently developed Transverse Coherence Minimization (TCM) method of Bishop et al. (2023). TCM minimizes the coherence between the infrasound and colocated transverse seismic component to detect air-ground coupled waves (AGCW) and determine the back–azimuth. We use 10 s data segments with 50% overlap and analyze data between 1–20 Hz on station SSLN and SSLS.

Discrete events (explosions) are detected in infrasound data using the network-based Short-Term Average/Long-Term Average (STA/LTA) technique (Allen 1978). VOISS-Net only classifies spectrograms in 2 min intervals, therefore it does not produce

Table 1 2023 Shishaldin eruption sequence seismic metrics.

Event number	Seismic Start	Seismic End	Seismic Duration [h]	D_R Peak Time	D_R Peak [cm^2]	Repose time [days]
1	23/07/14 08:30	23/07/14 10:30	2	23/07/14 09:55	19.8	
2	23/07/15 23:45	23/07/16 07:45	8.0	23/07/16 06:15	24	1.8
3	23/07/18 07:53	23/07/18 17:00	9.1	23/07/18 15:53	20.6	2.4
4	23/07/22 07:35	23/07/23 09:30	25.9	23/07/23 08:13	38.1	4.7
5	23/07/25 22:45	23/07/26 21:00	22.3	23/07/26 17:33	15.4	3.4
6	23/08/03 18:00	23/08/04 22:45	28.7	23/08/04 22:04	23.9	9.2
7	23/08/14 21:31	23/08/15 11:40	14.2	23/08/15 10:42	26.3	10.5
8	23/08/25 06:00	23/08/26 01:14	19.2	23/08/26 00:38	15.7	10.6
9	23/09/05 11:00	23/09/05 20:40	9.7	23/09/05 18:55	24.1	10.8
10	23/09/15 12:00	23/09/16 06:00	18.0	23/09/16 01:51	31.3	10.3
11	23/09/22 12:00	23/09/25 20:00	80.0	23/09/25 13:43	26.1	9.5
12	23/10/03 05:00	23/10/03 17:00	12.0	23/10/03 13:49	20.2	8.0
13	23/11/03 03:00	23/11/03 15:30	12.5	23/11/03 04:56	3.5	30.6

Table 2 2023 Shishaldin eruption infrasound metrics. No infrasound was detected for Events 7 and 9, as indicated by the "nd" for no detection.

Event number	Infrasound Start	Infrasound End	Infrasound Duration [h]	Infrasound Peak Time	RMSp Peak [Pa]	Number of explosions	Peak explosion rate (explosions/ 5 min)
1	23/07/14 05:31	23/07/14 11:25	5.9	23/07/14 10:00	4.9	1173	28
2	23/07/16 00:08	23/07/16 07:20	7.2	23/07/16 06:20	6.1	596	24
3	23/07/18 09:17	23/07/18 16:50	7.5	23/07/18 16:25	10.0	784	25
4	23/07/22 13:17	23/07/23 08:32	19.3	23/07/23 08:15	5.1	773	17
5	23/07/26 09:26	23/07/26 19:10	9.7	23/07/26 14:46	2.8	994	21
6	23/08/04 01:24	23/08/04 16:35	15.2	23/08/04 15:06	2.9	388	10
7	nd	nd	nd	nd	n/a	n/a	n/a
8	23/08/25 13:00	23/08/26 02:17	13.3	23/08/26 00:28	2.6	947	8
9	nd	nd	nd	nd	n/a	n/a	n/a
10	23/09/15 23:04	23/09/16 05:28	6.4	23/09/16 01:45	3.9	74	9
11	23/09/24 20:38	23/09/25 14:30	17.9	23/09/25 13:22	2.0	585	15
12	23/10/03 03:36	23/10/03 16:22	12.8	23/10/03 13:48	1.7	1	1
13	23/11/03 02:57	**23/11/03 15:02**	12.1	23/11/03 04:25	0.3	10	2

a complete discrete event catalog. Additionally, we only apply VOISS-Net to seismic data. We process infrasound data starting 30 min before and ending 30 min after the assessed infrasound start and end time, respectively. Explosions are detected using the recursive STA/LTA network trigger tool in ObsPy (Beyreuther et al. 2010). The network trigger uses all available infrasound stations for each event. Due to station outages and SSBA response issues discussed in Section 2.1, 7 events (1–6, 8) had one usable station (SSLS) while 4 events (10–13) had two usable infrasound stations (SSLS and SSLN). Infrasound data are processed by first applying a 0.5 Hz high-pass,

causal filter. We use STA and LTA windows of 1 and 5 s, respectively, an STA/LTA "trigger on" threshold of 2.5 and "trigger off" threshold of 2.0. Explosions must have a minimum peak pressure of 0.25 Pa or are discarded due to the high probability of spurious noise detections at low background noise levels. Acoustic travel time is removed between the station and the vent to align the waveforms. Explosion rates are then calculated in 5 min intervals.

We refer the reader to Loewen (this issue) for an overview of the 2023 eruption sequence, and to the various discipline-specific papers in this special issue for more details. Here we view each explosive event from 1–12 as a "paroxysm" while we suggest Event 13 represents a more modest explosive eruption based on the observed emissions and lower seismoacoustic signals.

3 Results

3.1 Event characterization

Broadband seismic tremor in March 2023 marked the earliest unrest for the 2023 Shishaldin eruption sequence. Figure 3 shows the AVO Aviation Color Code, D_R, SSLS seismic spectrogram, and binned VOISS-Net classifications between January 1, 2023–September 1, 2024. Clear broadband tremor is present in the spectrogram and VOISS-Net classification starting in late March 2023. This weak tremor continues until mid-April, then is present intermittently over the next few months. LP event classifications are also present before and after the broadband tremor and are common at Shishaldin during non-eruptive periods. Closer inspection of these LP classifications suggest many are real but some misclassifications also exist. The Explosion classifications in March–June 2023 are incorrect; VOISS-Net sometimes confuses LPs and transient data spikes with Explosions, a limitation that has been identified and discussed in both Tan et al. (2024) and Fee et al. (2025). Few Earthquakes are detected, consistent with the AVO catalog, and Harmonic and Monochromatic Tremor are essentially absent the entire period. Noise is the dominant class prior to and after the broadband tremor episode in March, up until Event 1. Station outages and low SNR in the first half of 2023 are primarily responsible for the misclassifications.

Notable similarities in the seismoacoustic amplitudes and spectral characteristics are present between the events. Figure 4 shows D_R alongside the seismic spectrograms for each event, while Figure 5 displays the RMS_p alongside the infrasound spectrograms. The seismic event onsets are marked by relatively broadband energy between ≈1–5 Hz, and this occurs for most events. Additional amplitude and spectral observations are discussed below with respect to the individual events.

3.1.1 Event 1

The first explosive event begins with a very subtle increase in seismic tremor around July 8. We note the amplitudes are low until July 14, and increase substantially at 08:30. Seismic amplitudes peak at 09:55 with a D_R of 19.8 cm^2 (Fig. 4). The seismic amplitudes decrease fairly rapidly and return to background by 10:30. Despite the earlier onset of tremor on July 8, we assign the Event 1 onset as July 14 08:30 as the

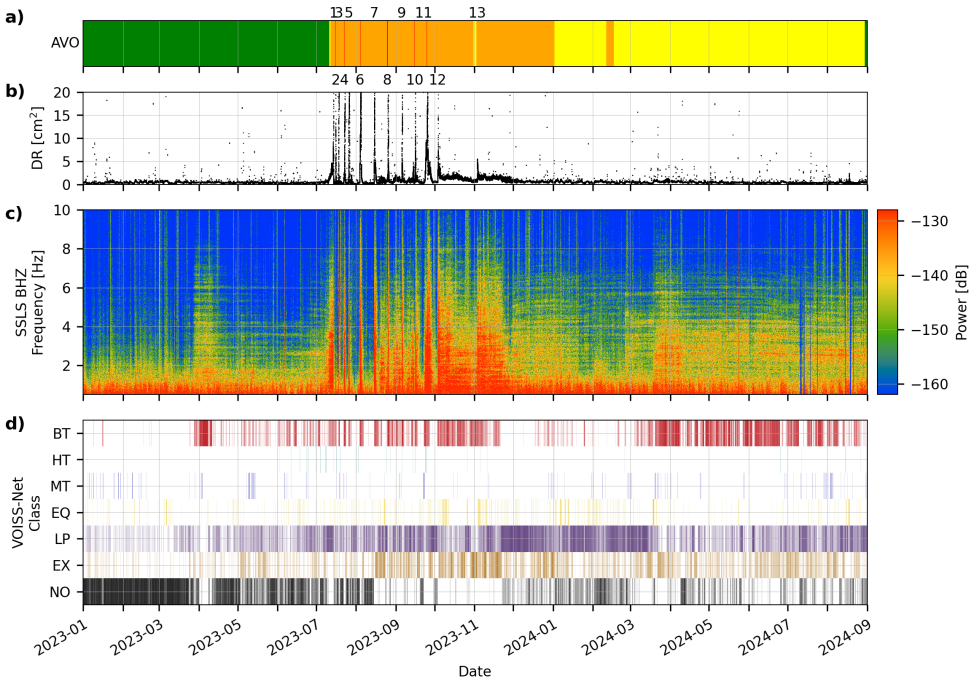

Fig. 3 Seismicity characterization surrounding the assessed 2023 Shishaldin eruption between January 2023–August 2024. a) AVO Aviation Color Code. Green=Normal background, Yellow=elevated unrest, Orange=heightened unrest or low-level eruption underway, and Red=significant eruption is imminent or underway. The 2023 explosive events are numbered. b) D_R for station SSLS. The plot is cropped at 20 cm^2 to highlight lower-level activity. c) Spectrogram for SSLS BHZ channel between 0.5–10 Hz. d) VOISS-Net classifications. Class labels on the left are abbreviated as: Broadband Tremor (BT), Harmonic Tremor (HT), Monochromatic Tremor (MT), Earthquake (EQ), Long Period (LP), Explosion (EX), and Noise (NO). Precursory BT is retrospectively detected in March 2023, and the large explosive events from July–November, 2023 are clear as rapid increases in D_R and BT. After the explosive eruptions, the seismicity gradually tapered off in amplitude and shifted from BT to predominantly LP and weak EX classifications.

earlier tremor looked similar to weak tremor episodes in the prior weeks and months. Event 1 infrasound begins on July 13 05:31 with weak, recurring discrete events (Fig. 5), but is perhaps occurring earlier and masked by wind noise. Infrasound amplitudes ramp up around 08:30 and peak at July 14 10:00 (essentially the same as seismic) with an RMS_p of 4.77 Pa. Similar to the seismic, the infrasound then drops off rapidly and ends by 11:25. The peak plume height is 11.6 km.

3.1.2 Events 2–4

The seismicity and infrasound for Events 2–4 all begin fairly abruptly and have similar trends (Tables 1 and 2, Fig. 4,5). Event 4 seismicity is much longer at 25.9 hr and has the highest D_R of the eruption at 38.1 cm^2. Event 3 has the highest RMS_p at 10.0 Pa. A decrease in peak infrasound frequency as the eruption progresses is present for

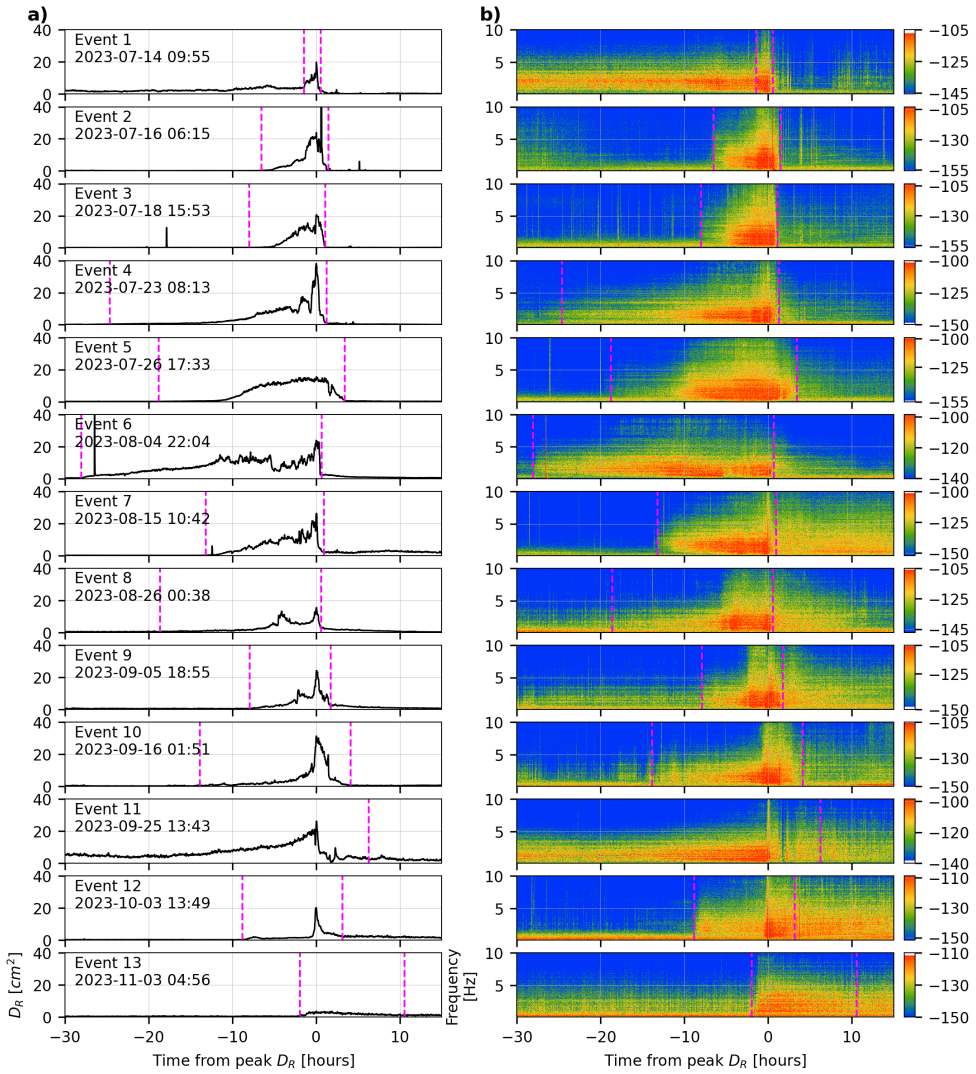

Fig. 4 Seismicity amplitudes (D_R) and spectrograms for the 13 explosive events. The magenta dashed lines indicate the eruption seismicity start and end times. a) D_R for SSLS aligned by the peak value, with the x-axis in hours from peak. The peak seismic amplitude time is noted by the timestamp. Non-volcanic regional earthquakes cause sharp spikes in D_R for Events 2, 3, 6, and 7. b) Spectrograms for SSLS BHZ from 0.5–10 Hz. Broadband tremor generally builds over the span of hours to days, and the peak typically contains higher frequency energy as well. Seismic run-ups range from approximately 1.4–74 hr prior to the peak value, with most below 15 hr. The seismicity tapers off more slowly for the events later in the sequence.

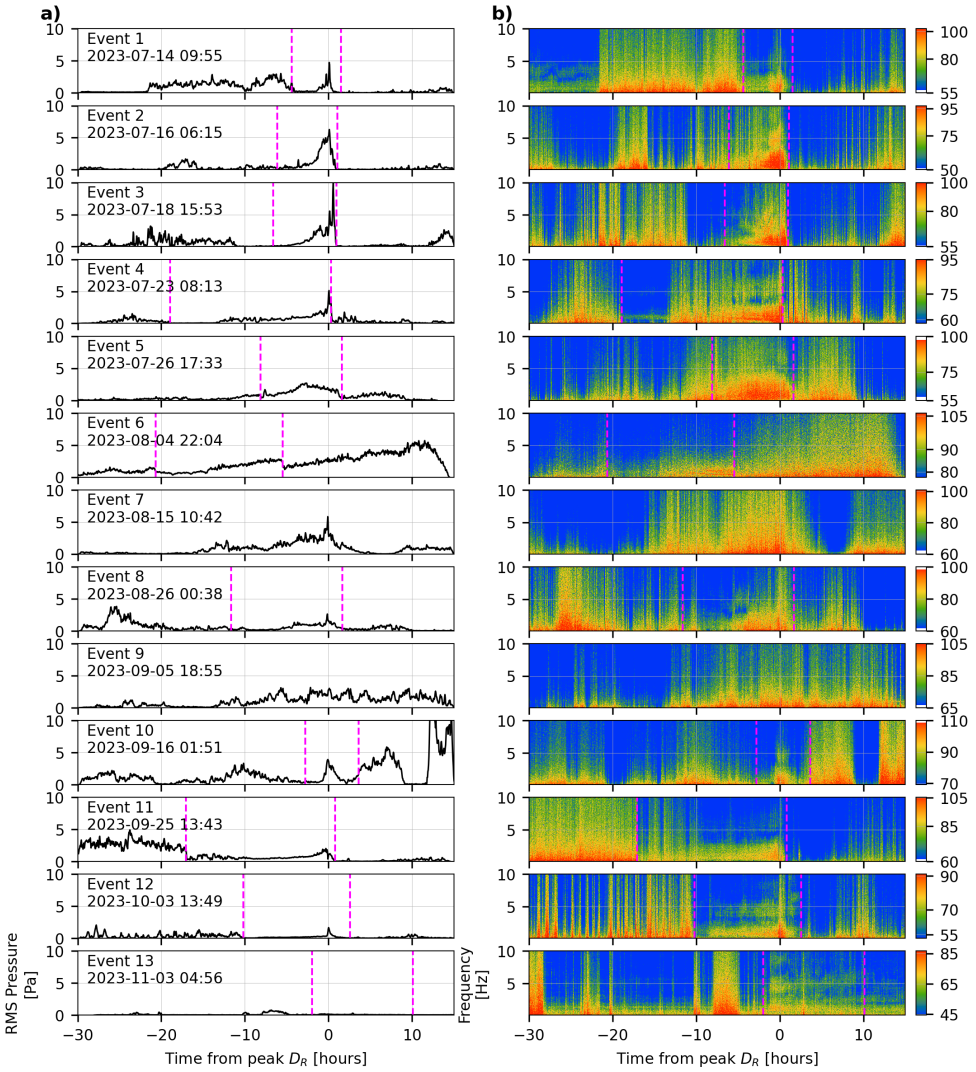

Fig. 5 Infrasound amplitudes and spectrograms for the 13 explosive events. The time axis and layout is the same as in Figure 4, except the dashed magenta lines indicate the eruption infrasound start and end times. a) RMS_p and b) spectrograms for SSLS BDF. No infrasound is identified for Events 7 and 9. Wind noise often dominates the infrasound records. RMS_p values outside the magenta lines are produced primarily by wind noise.

Event 4 and potentially other events. This is likely related to a decrease in the inter-event time between discrete explosions, as has been observed during Etna paroxysms (Ulivieri et al. 2013). The ash plumes from Event 2–4 have peak heights of 5.2, 7.9, and 13.7 km, respectively.

3.1.3 Event 5

Event 5 represents a change in seismoacoustic character. Events 1-4 have different seismic durations and amplitudes, but all have a relatively similar D_R shape where D_R increases subtly to form an initial peak (or two) (Fig. 4). Event 5 seismic and acoustics amplitudes increase starting around 06:00 and 09:26, respectively, but never reach a clear maximum. The amplitude envelope has a broad shape and relatively lower values of 15.4 cm^2 and 2.8 Pa. The ash plume height is also lower at 5.2 km.

3.1.4 Event 6–10

Events 6–10 have relatively similar seismic trends. D_R rises over a period of hours, often having a double peak separated by a few hours. Event 6 had a much longer seismic duration of 28.7 hr. Maximum D_R values range from 15.7–31.3 cm^2. Infrasound from these eruptions is not identifiable for Events 7 and 9, and Events 6 and 8 have relatively low peak amplitudes of 2.9 and 2.6 Pa, respectively. Plume heights range from 8.8–12.8 km.

3.1.5 Events 11–12

A notable change in the seismoacoustic signals occurs starting at Event 11, as the the amplitudes taper very slowly after the peak values. Event 11 begins with a subtle appearance of broadband tremor on September 22 at ≈12:00. The amplitude gradually rises and levels off after ≈24 hr, then begins to climb more rapidly on the 25th. Signals consistent with surficial flows are apparent in the seismic data, particularly between September 25 08:00–11:00. These signals have emergent, tapered waveforms with broadband spectra and are more apparent on SSLN to the north of the vent. D_R continues to climb and reaches high levels (≈20 cm^2) by 13:15. The seismicity then decreases briefly and the paroxysmal phase of the eruption begins at ≈13:35 with an emergent increase in broadband seismic energy, coincident with a large, rapidly rising plume to 14.7 km. D_R peaks at 26.1 cm^2 at 13:43. Seismic tremor levels then drop substantially, and sustained seismic tremor continues for another hour and then becomes more intermittent. In contrast to previous events, elevated seismic tremor and transient explosions then continue for more than two days. The duration of the eruption seismicity is approximately 80 h. The infrasound timeseries for this event has a very similar shape to the seismic and peaks at 13:22 at 2.0 Pa. The character of the infrasound changes markedly at 13:35, from repeated explosions to sustained low frequency tremor, which we attribute to jetting (Fee et al. 2010). Broadband infrasound continues until 14:30, when the infrasound then drops off rapidly and occasional discrete pulses (Strombolian explosions) are apparent for the next couple hours and appear to correlate with weak ash emissions apparent in satellite imagery (Gomez-Patron et al. this issue). A notable very low frequency signal is apparent in the seismic and infrasound data during the paroxysmal phase. This signal has a dominant period of ≈14 min and is visible in infrasound and seismic stations across Unimak Island after the full instrument response has been removed (Supplemental Figure 1). The signal begins around 13:35 and coincides with the transition to broadband seismic and infrasound signals, as well as heightened ash emissions and volcanic lightning. The propagation velocity

of this signal is very low (around 10 m/s), suggesting it is an internal gravity wave. Haney et al. (this issue) discuss this observation and model the signal as due to rapid injection of mass into the atmosphere, and from this they are able to derive a realistic mass eruption rate and total erupted mass. Previous work has related these waves with energetic volcanic plumes and derived mass eruption rates (Ripepe et al. 2016).

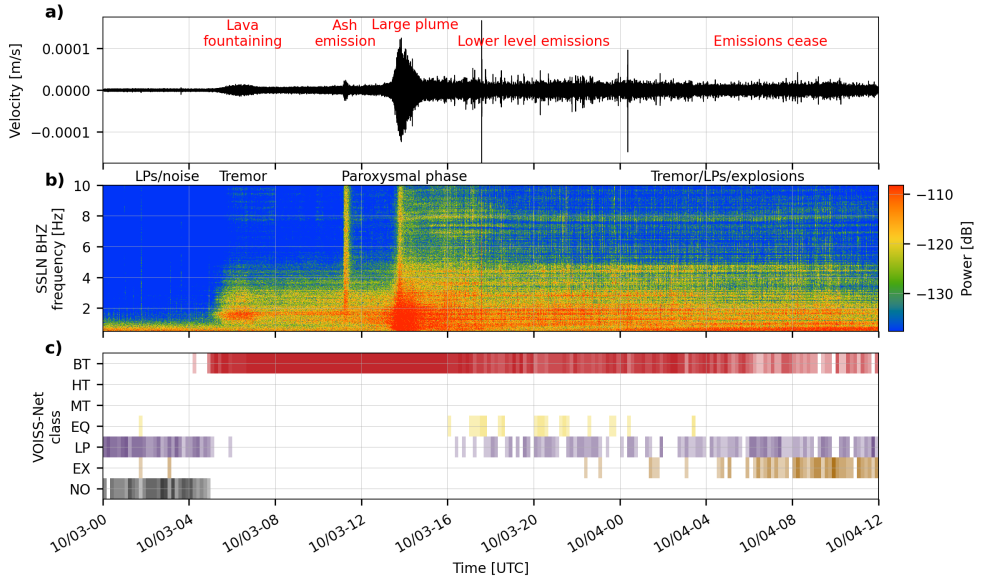

Fig. 6 Event 12 seismicity on Oct. 3–4, 2023. a) Waveforms from SSLN annotated with visual and remote sensing observations. b) Spectrogram for SSLN, annotated with various signal interpretations. c) Binned VOISS-Net classifications, similar to Figure 3 but binned in 10 min intervals. The eruption seismicity begins with a transition from LP to BT, with low-level fountaining visible in webcam views. The seismicity builds over a span of hours with increasing ash emissions. After the paroxysmal phase, the seismicity transitions from BT to a mix of LP, EQ, and EX.

Event 12 has considerable similarities to Event 11. Figure 6 displays the SSLN waveforms, spectrogram, and binned VOISS-Net classifications. The classifications are binned into 1 hr intervals and separated into class-specific rows, with the plotted bin opacity computed as the ratio of the class occurrence relative to the total number of time steps per hour. Broadband tremor between ≈1–5 Hz begins around October 3 05:00, as noted by a change from LP and Noise classifications, and continues until ≈12:00. Lava fountaining is observed during this period in rare clear webcam views. A broadband seismic increase from 11:15–11:30 coincides with a weak ash emission. This increase is primarily seen on SSLN, suggesting a surficial mass flow to the north side of the volcano that fed an ash plume. At ≈13:30 seismic amplitude rises steeply and peaks at 13:49 and 20.2 cm^2 for around 10 minutes, then begins a very gradual decline over the next hours to days (Fig. 4,6). Infrasound amplitude trends closely follow that of the seismic, peaking at 13:48 at a relatively low 1.7 Pa (Fig. 5). Infrasound

signals are notably continuous during this event and do not consist of discrete events. Similar to Event 11, a low frequency gravity wave was also produced around 13:45 and recorded across Unimak Island. The post-eruption seismicity stays above the pre-event background until the next event and consists of a mix of broadband tremor, LPs, weak explosions, and occasional VT earthquakes. The VT earthquakes are somewhat unusual for the sequence and range between -2–5 km depth beneath the summit with magnitudes between M_L 0.9–2.2. Supplemental Figure 1 shows the unfiltered, 0.5–10 Hz, and gravity wave (20 min to 10 s) characteristics of Events 11 and 12 as recorded on the SSLS infrasound station.

3.1.6 Event 13

The final explosive event on November 3 (Event 13) is much weaker than the others. The seismicity and infrasound peaks are at 3.5 cm^2 and 0.3 Pa, which are the lowest of the explosive events. The plume is also ash-poor and rose to only 6.1 km. Seismicity before and after the event is relatively high with D_R ≈1 cm^2, and took weeks to decrease to lower levels (Fig. 3).

3.1.7 Event Repose Time and Post-eruption Signals

Some of the event repose times are remarkably regular. Table 1 lists the elapsed time in days between each eruption. Events 2–5 occur between 1.8–4.7 days after the previous event. Events 6–12 then occurred between 8.0–10.8 days after the previous event, with Events 7–9 showing a remarkably stable repose time of 10.3–10.8 days. This allowed AVO to issue forecasts for multiple events. Event 13 then has a much longer repose time of 30.7 days, which may be related to its lower explosivity and geophysical parameters and suggests a decrease in gas and magma supply. The duration of seismicity does not seem to correlate with the repose time (Table 1).

After the final explosive event, the seismicity and infrasound continue at relatively low levels for months (Fig. 3). The seismicity generally consists of a mix of discrete but repeating LP events that are occasionally classified as Explosions or Broadband Tremor. D_R values stay low (<1.5 cm^2) through 2024. An increase in broadband tremor is apparent in March–April 2024, and some long-term, weak spectral peaks are present in the spectrograms (Fig. 3c). Discrete, repeating infrasound events are also present through the rest of 2023 and 2024, and are linked to the seismic LP events. These events are generally weak (<0.5 Pa), last less than 10 s, and have a broadband onset followed by more monochromatic coda.

3.2 Acoustic–seismic coupling

During the eruption, seismic frequency content changed around the paroxysmal phase for many events, as there was a shift to more broadband seismicity with greater high frequency energy. This is apparent for most events around hour "0" in Figure 4 and visible in Figure 6 at ≈11:15–11:30 and ≈13:45–14:15. The shift is more apparent on SSLN and SSBA than SSLS. TCM application to colocated seismoacoustic stations reveals that this spectral shift is related to acoustic waves coupling into the ground and being recorded on the seismometer. Figure 7 shows the Event 10 seismoacoustic

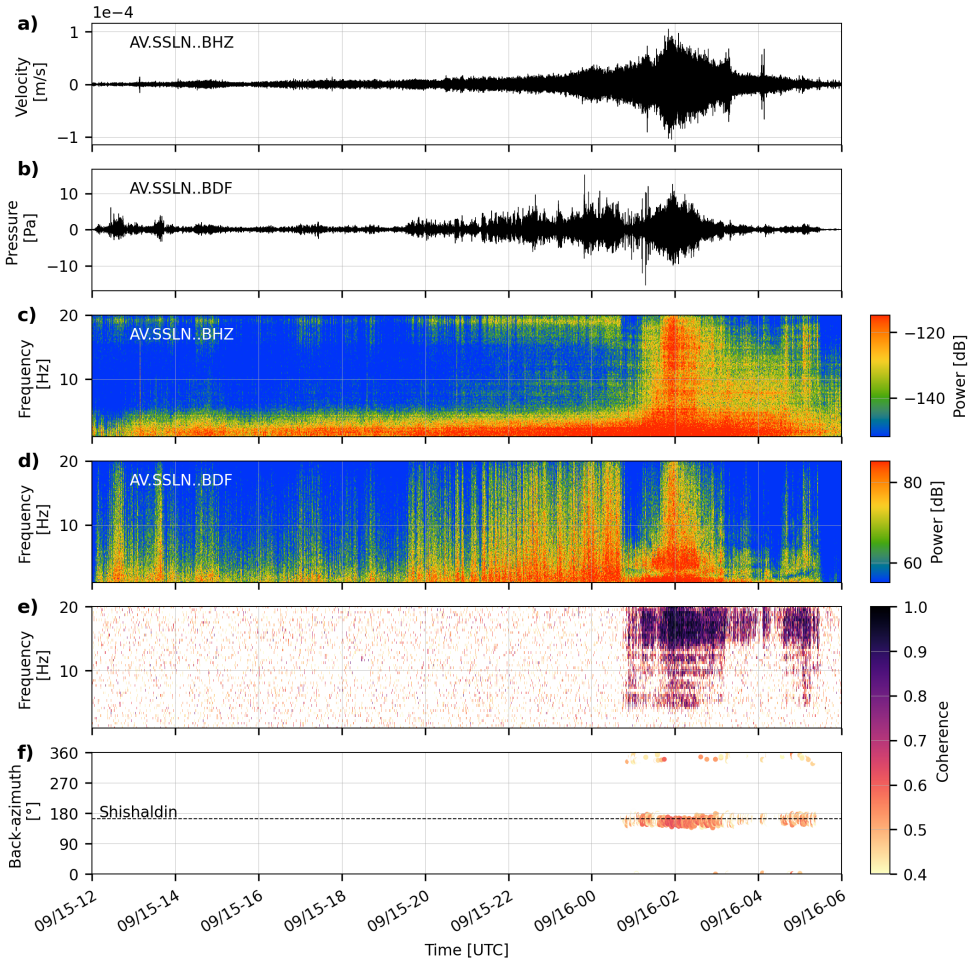

Fig. 7 Transverse Coherence Minimization (TCM) for Event 10 on September 15–16 computed at SSLN. a) Seismic and b) infrasound waveforms between 1–20 Hz and c) seismic and d) infrasound spectrograms. e) Coherence between the infrasound and vertical seismic record, showing clear coherence between ≈5–20 Hz during the paroxysmal phase. f) TCM-derived back-azimuth, illustrating that the incident acoustic waves during periods of high coherence are originating from Shishaldin, indicated by the dashed horizontal line. The back-azimuth is colored by the mean coherence between 1–20 Hz shown in e).

data and TCM results for SSLN. The paroxysmal phase (≈01:45–02:15) has similar seismic and acoustic characteristics and frequency content. The bottom two panels show the acoustic-seismic coherence and TCM-derived back-azimuth. The clear shift to broadband seismicity from 5 to at least 20 Hz corresponds to high coherence between the two sensors in this band. The TCM algorithm assumes retrograde motion by default, but upon further inspection the particle motion at SSLN above ≈12 Hz is prograde. Therefore for this case we modify TCM to choose the prograde solution.

Supplemental Figure 2 displays the frequency-dependent particle motion at SSLN for Event 10 and discusses this in more detail. The TCM-derived back-azimuth for this period is around 160 °, consistent with the geographic back-azimuth from the station to the summit (164 °), confirming the waves are AGCW and originate from Shishaldin. This is consistent with research by others (e.g., Ichihara et al. 2012; Matoza and Fee 2014), that demonstrates how energetic infrasound from volcanic eruptions can be recorded on seismometers and why colocated acoustic sensors are useful for accurate interpretation. The AGCW does not seem to have an appreciable effect on the D_R calculation, as the majority of the coupling is above 10 Hz and most of the seismic energy is focused between 1–2 Hz.

3.3 Infrasound characterization

While the seismicity from the Shishaldin eruption shares similar characteristics between events, some infrasound features contain notable variability. The RMS_p curves in Figure 5 typically show a build-up in amplitude over the scale of hours, with variable peak values between 2–10 Pa. The spectral characteristics are also somewhat similar with energy concentrated between ≈1–3 Hz until the paroxysmal phase. Figure 8a overlays the D_R and RMS_p for Event 4 on July 23. The amplitudes from both datasets follow similar trends and peak around 08:15. Closer inspection of the waveforms, though, shows differences between the seismic and infrasound characteristics. Figure 8b-c displays 2 min of data band-pass filtered between 1–10 Hz during the eruption build-up (04:26–04:28) and Figure 8d-e shows 2 min of data during the paroxysmal phase (08:15–08:17). A large ash plume emitted to 12–14 km was observed around 08:10–08:20 compared to no obvious plume until 05:20 (Gomez-Patron et al. this issue). The seismic waveforms during both periods look similar and consist primarily of sustained broadband tremor, with amplitudes around 08:15 approximately double that of 04:26. Conversely, the infrasound during both periods consists primarily of discrete events of variable amplitudes and inter-event times. The infrasound during the paroxysmal phase does have higher amplitude (up to 45 Pa peak-peak compared to roughly 12 Pa peak-peak) and more frequent explosions. These observations are notable for the following reasons: 1) Despite similar amplitude trends, the character of the seismic (continuous) and infrasound (discrete), are markedly different. 2) Existing models of seismoacoustic signals for paroxysms at basaltic stratovolcanoes, such as Etna (Ulivieri et al. 2013; Vergniolle and Ripepe 2008) and the 1999 Shishaldin eruption (Caplan-Auerbach and McNutt 2003; Thompson et al. 2002), suggest that the eruption transitions from discrete to continuous infrasound signals during the paroxysmal phase. Figure 8 highlights that despite a notable change in the ash plume height (and other eruption parameters), this paroxysmal phase consisted primarily of discrete, energetic Strombolian explosions, similar to the second Strombolian phase in the 1999 eruption (Vergniolle et al. 2004)

Analysis of the amplitude and rate of discrete infrasound signals from all 13 events show multiple different styles exist at Shishaldin. Figure 9 displays the event rates and maximum pressure of discrete infrasound signals detected using the network-based STA/LTA technique. We plot these metrics in hours from -20 to +5 hr of the peak D_R

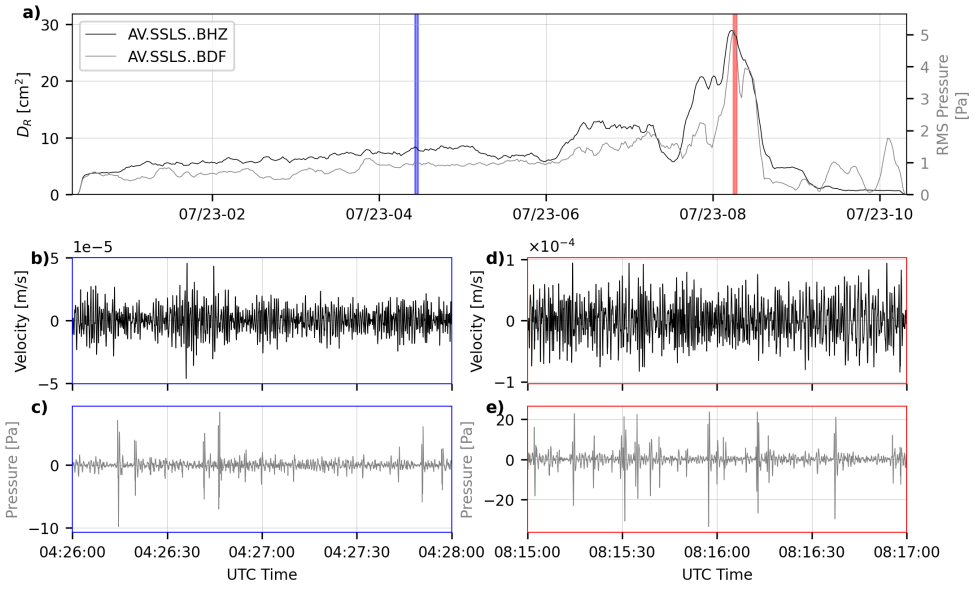

Fig. 8 Seismoacoustic characteristics of Shishaldin Event 4. a) Seismic (black) and infrasound amplitudes (gray) over time, followed by b) seismic and c) infrasound waveforms during the eruption build-up and d) seismic and e) infrasound waveforms from the eruption peak. Blue and red boxes indicates the time period in a). Notably, the seismic character consists of sustained broadband tremor during both periods while the infrasound is composed primarily of discrete explosions, even during the paroxysmal phase noted in red.

(Table 1). Based on the trends in these metrics and visual analysis, we sort and plot the events into three groups and describe the general infrasound characteristics:

Group 1 (Events 2, 3, 4, 11): Discrete explosions that increase in rate and amplitude over time with little to no sustained signals. All events have high peak explosion amplitudes between 37.1–72.2 Pa at SSLS. Event rates peak between 15–25 events per 5 min. The peak event rate and amplitudes generally coincide with the D_R maximum. All four events in this group have similar characteristics.

Group 2 (Events 1, 5, 6, 8): A mixture of discrete and sustained infrasound signals. This group has moderate peak amplitudes between 15.16–44.5 Pa and peak event rates between 9–28 events per 5 min. The maximum pressure and event rate occurs at different periods for the various events, and the events in this group have relatively variable characteristics.

Group 3 (Events 12, 13): Sustained signals with essentially no discrete events. These two events contained markedly different infrasound characteristics than the other events.

We discuss the implications of the explosion detections and inferred eruption dynamics in Section 4.

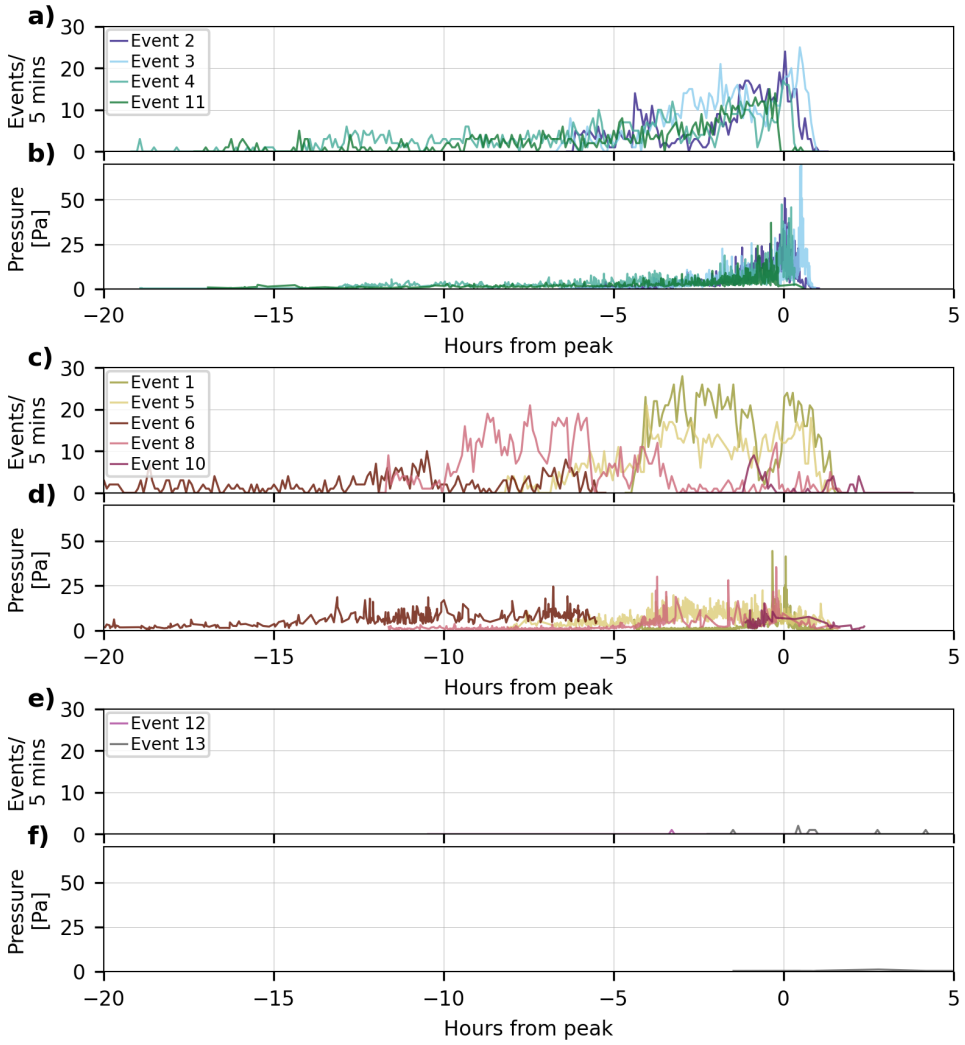

Fig. 9 Infrasound explosion detections. The explosion event rates and pressures are placed into three groups based on similar characteristics and plotted relative to the time from the peak D_R, similar to Figures 4 and 5. Group 1 events are shown in a) and b), Group 2 in c) and d), and Group 3 in e) and f). Group 1 consists of relatively similar events that have gradual increases in event rate and pressure. Group 2 events show more variability with a mix of event rates and pressure. Group 3 has just a few discrete explosions with very low pressure values, so panels e) and f) are mostly empty.

4 Discussion

4.1 Comparison to Past Explosive Eruptions

Compared to past eruptions, the 2023 unrest was notable for the numerous energetic explosive events and the relatively similar inter-event time and seismoacoustic trends. The 1999 eruption sequence had two paroxysms on April 19 and 23, with the latter being more energetic seismically but having a lower plume height (Nye et al. 2002). These two events had peak D_R values of 23 and 43 cm^2 (Thompson et al. 2002), respectively, which are of a similar range to the peak D_R during the 2023 sequence (Table 1, Fig. 4). The April 19 eruption had an 80 min energetic Subplinian phase, as determined via seismic data, and ≈12 h of elevated seismic tremor. This Subplinian phase produced energetic infrasound for ≈50 min (Caplan-Auerbach and McNutt 2003; Vergniolle and Caplan-Auerbach 2006). The April 23 eruption was primarily Strombolian in nature, with a slightly higher D_R of 43 cm^2 (Thompson et al. 2002) compared to the 2023 peak of 38.1 cm^2 during Event 4. Note, however, that Thompson et al. (2002) compute D_R using a combination of body and surface wave spreading factors. We recomputed D_R for the 1999 eruption using the approach described in Section 2.2 and find slightly higher peak values for station SSLW of 29 and 52 cm^2. The 1999 eruptions both had slow tremor build-up and relatively rapid drop-off (Thompson et al. 2002). These trends are quite similar to the 2023 Events 1–10. Events 11–13 had a more gradual return to background, with seismicity staying elevated until the next explosive eruption. Tremor spectral characteristics are similar between 1999 and 2023, with broadband tremor focused between ≈1–5 Hz. The inferred Subplinian phases in 1999 had a shift to more broadband signals, with considerable energy above 5 Hz. We assume this change is related to energetic AGCW being recorded by the seismometer, similar to the 2023 paroxysms (Fig. 4, 7). Based on the seismic similarities between the 1999 and 2023 paroxysms, we assume similar source processes and models, at least for Events 1–10 in 2023. Both the 1999 and 2023 eruption sequences had precursory seismicity in the months before the explosive phase, with tremor being recorded ≈3 and 4 months prior, respectively.

Multiple episodes of energetic Strombolian explosions were also observed in the seismic and acoustic data during the 1999 eruptions (Thompson et al. 2002; Caplan-Auerbach and McNutt 2003; Vergniolle et al. 2004). Four sequences of vigorous, discrete events were observed between the April 19 and 23 Subplinian eruptions. Weaker discrete events were detected before and after the eruptions. These sequences were all predominantly gas-rich. A 2–3 Hz acoustic "hum" was only recorded in the build-up to the April 19 Subplinian eruption, and we do not observe this signal in 2023. Weak, repeating infrasound signals prior to some events (e.g., Events 1 and 4, Fig. 5b) produce some diffuse energy between 1–3 Hz, but we believe this is different than the more energetic hum reported for the 1999 eruption.

The seismoacoustic data from the 2019–2020 eruptions have not been studied in detail, but share some similarities with the 2023 eruption signals. Loewen (this issue) provides a broad overview of the seismicity from the three explosive eruptions in January 2020. These three events had seismic tremor build-ups that lasted between ≈2–25 hr and peak D_R values between 8.1–18.5 cm^2. These values are similar in range

to those observed during the 2023 eruption sequence, with the D_R values on the lower end of those observed in 2023. Notable infrasound signals from the 2019–2020 eruption sequence were picked up intermittently on regional infrasound arrays, although data outages and strong wind noise limited some of the observations. Ash plume heights were also on the lower–middle end of those observed in 2023 (7.0–9.8 km). In contrast to other recent eruptions, this sequence also had effusive periods which fed a lava flow down the north flank of the volcano. Effusive episodes between October–December 2019 had D_R trends similar to many of the 2023 explosive events. We leave a more detailed analysis of the 2019–2020 seismoacoustic signals to future work.

Weak, discrete seismic and infrasound signals were recorded for years after the 1999 eruption. Petersen and McNutt (2007) detail these signals for the 2003–2004 time period and modeled them as shallow, steam-rich explosions that produce weak LP seismicity and discrete infrasound. The seismoacoustic signals after the 2023 eruption that occurred in 2024 and continue at the time of writing resemble these events, as well as others regularly detected by AVO in the intervening years. We assume the late 2023–current seismoacoustic signals to be the result of shallow, discrete gas release from magma and fluids related to the 2023 eruption, but cannot rule out the intrusion of new magma to shallow depths as the source. Elevated SO_2 has been regularly detected alongside heightened LP activity (Lopez et al. this issue), suggesting a magmatic instead of a hydrothermal source. More detailed analysis of these signals, combined with visual, thermal, and gas observations, could provide insight into shallow degassing processes, similar to Petersen and McNutt (2007). We note that sustained tremor appears as a precursory signal prior to the 1999 and 2023 eruptions, while LP events occur more as "normal, background activity" before and after the explosive phases.

4.2 Seismicity trends and source models

Although some variability exists in the seismicity for the 2023 eruptions, we suggest the source process driving the seismicity and explosive events is relatively consistent throughout the eruption. The broadband seismic tremor and transient events showed little change in spectra over time (Fig. 3, 4). Nearly all events had a gradual amplitude rise and more rapid decrease, which follows a similar amplitude versus time trend to many Etna paroxysms (Andronico et al. 2021). Detailed seismicity source modeling is beyond the scope of this manuscript, but we envision the broadband eruption tremor in 2023 to be related to flow-related turbulence and erosion within the shallow conduit (Fee et al. 2017; Gestrich et al. 2020; Coppess et al. 2025), as significant erosion of the crater rim occurred between Events 8–12 and possibly within the conduit during earlier events. Girona et al. (this issue) propose an alternate model of the Shishaldin tremor as the result of pressure oscillations from a shallow gas pocket based on the original model presented in Girona et al. (2019).

The regular repose times in 2023 provide insight into deeper source processes driving the eruptions. Events 1–5 exhibited similar seismic build-ups and repose durations (Fig. 4; Table 1). Event 5 was atypical: rather than a sharp pre-event seismic maximum, it displayed a long, broad amplitude plateau, and its plume height was lower (around 5 km). After this event, the inter-event durations lengthened and became strikingly uniform for Events 6–12. Vergniolle (2024) used laboratory-informed models,

seismoacoustic data, and previous studies of the 1999 eruption to propose a two-foam system: a radially extensive foam accumulating at the top of the magma reservoir under a steady deep gas flux, and a long foam developing within the conduit. The reservoir foam, being close to its limit of stability, is capable of forming "trigger bubbles", while infrasonic "hums" observed prior to the 1999 Subplinian phase were interpreted as repeated bubble bursting associated with coalescence within the conduit foam. The ascent of the trigger bubble through the conduit then disrupts the conduit foam, leading to extensive fragmentation and Subplinian activity. The 2023 sequence is qualitatively compatible with this mechanism: a near-constant recharge rate between July and November would build the foam to threshold on a quasi-periodic timescale, yielding regular inter-event intervals, while variability (e.g., Event 5) may reflect transient changes in near-vent permeability or melt rheology (Bamber et al. 2024). However, no sustained infrasonic hum was recorded between events in 2023, and its absence might suggest a comparatively low-leakage, well-sealed conduit system compared to that which was inferred for 1999. A full quantitative evaluation of the eruption source mechanisms is left for future work.

The notable change in seismicity after Event 11 is consistent with other datasets and suggests shallow dike intrusion during this interval disrupted the system. Visual observations documented the development of an eroded "notch" at the previously conical summit beginning in August 2023 (around Event 8) (Loewen this issue). Over subsequent weeks this notch enlarged into a NE–SW trending depression up to 100 m deep and ≈1 km long, incising a valley at Shishaldin's summit (Angarita et al. this issue). Starting with Event 11, SO_2 was also detected between eruptions rather than solely during them, indicating more continuous shallow degassing (Lopez et al. this issue). Deformation observations and modeling likewise support shallow intrusion during this period (Angarita et al. this issue). Taken together, these observations suggest that Events 11–13 were sourced by shallower magma that continued to degas between explosive episodes. This more persistent near-surface degassing plausibly produced the broadband tremor, LPs, and weak explosions observed near-continuously in the seismoacoustic data between Events 11 and 13, and the elevated tremor persisted well into 2024 (Fig. 3, 5, 6). The shallow dike may have also contributed to increased conduit permeability, weakening or partially bypassing the conduit foam, and allowing more continuous gas escape to the surface.

The seismicity from the explosive events in 1999, 2019–20, and 2023 all consist of increases in broadband tremor amplitude prior to the paroxysmal eruption phases (Fig. 3, 4). Most of the events began with a transition from repeating, weak LPs to broadband tremor (e.g., Fig. 3, 6). These key observations allowed AVO to forecast multiple events in 2023, and assisted with real-time monitoring. The use of VOISS-Net facilitated near-real-time and post-event analysis by permitting fast, repeatable seismicity detection and classification, although some misclassifications occurred. Girona et al. (this issue) describe two methods for using the seismic amplitudes and other parameters in a data assimilation technique to provide quantifiable eruption forecasts, and we view these types of methods as promising for future monitoring and hazard mitigation at Shishaldin. Additionally, the appearance of higher frequency, sustained seismicity from AGCW (Figure 4, 7, 6) and energetic infrasound also suggests the

utility of closely monitoring infrasound signals for detection and characterization of the paroxysmal phase.

4.3 Gas flow and eruption dynamics inferred from infrasound

Changes in basaltic eruption dynamics are often assumed to result from different two phase magma-gas flow regimes, in particular the rate and mechanism of gas flow (e.g., Wilson 1980; Vergniolle and Jaupart 1986; Houghton and Gonnermann 2008; Pioli et al. 2012; Spina et al. 2019). Idealized views of the dominant gas flow regimes at basaltic volcanoes have been related to their subsequent eruption styles. The low viscosity of these magmas allow for two phase flow (gas and magma). At low gas fluxes and magma ascent rates, small bubbles are able to uniformly rise through the conduit with little interaction and overpressure, termed "bubbly flow", and produce passive degassing at the surface. At higher gas flow rates, the bubble density is non-uniform and the bubbles interact and coalesce. Pressurized gas slugs may form and then erupt to produce Strombolian explosions. As gas flow rate increases, the regime changes to churn and eventually to annular flow, which is characterized by unsteady flow with a high fraction of gas to magma. Churn and annular flow produce vigorous lava fountaining, and likely sustained paroxysmal eruptions that can produce Subplinian eruptions (e.g., Houghton and Gonnermann 2008). Recent evidence suggests that changes in viscosity may also play a role in eruption style, slug ascent and recurrence rate, as well as seismic amplitude (Spina et al. 2019; Longpré et al. 2025) for these types of eruptions. We also note that ascent rate variability likely also plays a role in eruption style, with high ascent rates being likely for basaltic Subplinian and Plinian eruptions (Parfitt 2004; Szramek 2016; Rasmussen et al. 2018; Bamber et al. 2024).

Clear links have been established between geophysical signals and gas flow regimes at basaltic and other volcanoes, as well as in laboratory experiments. Fee and Matoza (2013) provide an overview of the various infrasound signal characteristics for different volcanic eruption styles. For example, Strombolian eruptions produce short-duration, impulsive infrasound while Subplinian eruptions typically produce high-amplitude, sustained infrasound resembling a low frequency form of jet noise. Infrasound signals provide direct measurements of the pressure release at the volcanic vent. Recent laboratory experiments by Spina et al. (2019) simulated various two-phase gas-liquid flow regimes by changing the gas flow rate and viscosity. They found that slug flow produced discrete seismoacoustic signals, and increasing the gas flow rate produced a higher slug burst rate observed in the acoustic data. This pattern was not apparent in the laboratory seismic data of Spina et al. (2019), and no clear trend in discrete seismic events was observed, likely due to the presence of additional seismic sources with no acoustic counterpart. High flow rates created churn-annular flow that produced near-continuous infrasound signals (tremor or jetting). In general, infrasound and seismic amplitudes were correlated with increasing gas flow rates, with possible modulation from magma viscosity. Seyfried and Freundt (2000) also found that increased gas flow rate caused a transition from slug to churn-annular flow in laboratory experiments of two-phase flow. The aforementioned observations and experiments suggest that acoustic signals can be a key indicator of the gas flow regime at basaltic volcanoes, while the seismicity may provide less information on the flow regime.

Building off work by Vergniolle and Ripepe (2008), Ulivieri et al. (2013) examined the infrasound signals from 39 Mt. Etna lava fountain paroxysms between 2007–2013. They found that the infrasound signals during these sequences begin as repeating low-amplitude, discrete signals from Strombolian explosions. As the sequence evolves, the infrasound signal amplitudes and event rates increase, eventually transitioning to sustained, high-amplitude infrasound. The seismicity also increases in amplitude over time similar to the infrasound, but remains relatively continuous without clear discrete events. Ulivieri et al. (2013) suggested that these transitions from discrete to continuous signals represent evolving gas flow regimes. The eruption starts as low-level, discrete Strombolian eruptions driven by repeating gas slugs. Over time the gas slugs increase in overpressure, possibly related to increased gas flux (Seyfried and Freundt 2000), causing the increase in infrasound amplitudes and decrease in recurrence interval. Eventually the gas flow regime evolves from discrete gas slugs to churn or annular flow, producing lava fountains and hazardous ash plumes, and continuous, high-amplitude infrasound signals. Notably, the seismicity does not reflect the change from discrete to sustained gas flow and release. Ripepe et al. (2018) used these trends in infrasound array data to devise an early warning system with a 96% success rate over their study period.

The infrasound signals from Shishaldin explosive events in 2023 show some similarities with those from Etna paroxysms, but contain some key differences. The Group 1 events (Fig. 9a,b; Events 2, 3, 4, 11) look most similar to the Etna paroxysms. These events generally have discrete signals that increase in acoustic amplitude and event rate over time, presumably from gas slug flow and subsequent burst. However, unlike Etna, Events 2–4 do not transition to sustained signals from churn-annular flow, and presumably the paroxysmal phase is driven primarily by energetic, discrete gas slugs. Lower-level sustained infrasound is likely present during many of the discrete phases (e.g., Fig. 8c,d), suggesting that the flow regime may be some combination of discrete and sustained gas release, which is possible under some churn flow conditions (Parfitt 2004). Group 2 events (Fig. 9c,d; Events 1, 5, 6, 8, 10) consist predominantly of discrete events but do not show clear amplitude and event rate trends. Additionally, the discrete events in this group are mixed with sustained signals. We suggest these events are driven by a more complex mix of slug and churn-annular gas flow. Group 3 events (Fig. 9e,f; Events 12 and 13) stand out for containing almost no discrete events and primarily sustained signals, suggesting that churn-annular flow is occurring for the majority of these events. Despite the continuous gas flow regime, the infrasound amplitudes are only moderately high for Event 12 (RMS_p peak of 1.66 Pa) and low for Event 13 (RMS_p peak of 0.2 Pa). The energetic paroxysm and gravity wave at the end of Event 11 may be an indicator of a change in the system towards more sustained infrasound.

Based on the assumption that discrete infrasound corresponds to slug flow and sustained infrasound from churn-annular flow, we suggest a single transition from slug to churn-annular flow did not occur for the Shishaldin 2023 explosive events, and that churn-annular flow is not needed to produce sustained, high ash plumes. This is consistent with observations and modeling for similar volcanoes. Lyons et al. (2010) noted paroxysms at Fuego Volcano, Guatemala, another basaltic stratovolcano, were

characterized by repeated explosions occurring at 0.5–3 s. Ichihara (2016) suggested that the 2011 Shinmoe-dake, Japan Subplinian eruption was also driven by repeated, shallow explosions rather than a sustained jet. A similar mechanism was invoked for the 2016 Pavlof Volcano, Alaska eruption by Haney et al. (2018). These results suggest that paroxysms at basaltic stratovolcanoes may result from multiple gas-magma flow regimes, and that variability in the subsequent seismoacoustic signals should be expected. We caveat our flow interpretation with the possibility that churn flow could potentially produce "violent Strombolian" explosions (Pioli et al. 2008) that have been suggested to drive moderate (2–6 km above the vent) plumes. Additionally, Parfitt (2004) and related work suggest that increased magma ascent rates may also be responsible for a transition from transient explosions to sustained explosive eruptions in basaltic magmas. The considerable variability in the acoustic signals during paroxysms at Shishaldin suggests additional work is needed to understand the gas flow regimes during explosive eruptions at basaltic volcanoes. Additionally, the seismicity from all 13 explosive events follows a more regular pattern of increasing amplitudes and sustained broadband tremor during each explosive eruption, and therefore seems decoupled from the variability seen in the infrasound and the inferred two-phase gas flow dynamics. This is generally consistent with laboratory studies (Spina et al. 2019) and observations at Etna (Ulivieri et al. 2013), and suggests a different source depth or process.

In summary, we suggest the 2023 seismoacoustic signals are sourced from a relatively steady deep gas flux that builds a radially extensive foam at the reservoir–conduit interface. When the foam reaches a critical thickness/overpressure and begins to collapse, the system begins a transition into an energetic Subplinian episode. Between events, intermittent LP events are produced by discrete slug releases propagating up through the conduit, whereas the broadband tremor during explosive eruptions reflects sustained, high-flux, two-phase flow fed by the collapsing foam. The later events in the sequence are influenced by a shallow dike intruding near the summit, which increases the near-surface permeability and provides a more efficient pathway to the surface, facilitating continuous gas release and background tremor and more frequent LPs between events. The infrasound signals have a more complex relationship and show greater variability, likely related to complex two-phase gas flow transitions during the foam collapse. Future work should focus on integrating quantitative models to verify the source processes and associated volcanic emissions.

5 Conclusions

Shishaldin volcano produced 13 explosive events between July–November, 2023. These events created significant ash plumes to over 14 km ASL and hazards to air traffic. The seismic and infrasound signals from these events were recorded well on a local geophysical network, and provide a rich dataset for understanding eruption processes. Classification of seismicity using a machine learning model produced an extensive catalog useful for identifying pre-, syn-, and post-eruptive seismicity and associated processes. We find that subtle, intermittent seismic tremor preceded the explosive

events by months. All explosive events are characterized by relatively similar seismicity: a change from repeating LP events to broadband tremor, which subsequently increases in amplitude over a span of hours to days. A complex mix of LPs, intermittent tremor, and weak explosions occurs between the events, with a low number of VT earthquakes. Early explosive events in the eruption sequence have a more gradual seismic run-up, while explosive events at the end have a longer cessation. This trend is consistent with other datasets that showed an influx of shallow magma and possible dike intrusion for the last few explosive events. The explosive events have fairly regular repose times on the order of days. Shishaldin eruption seismicity in 2023 is similar to past explosion eruptions in 1999 and 2019–20, although the higher number of explosive events and relatively similar repose times are notable differences.

The infrasound from the explosive events is more variable and provides some unique insight into gas flow and eruption dynamics. The explosive events produced a varied mix of discrete explosions and sustained infrasound signals. At Etna, similar paroxysms are inferred to result from a transition from gas slug to churn-annular two-phase flow. In contrast, we suggest the Shishaldin 2023 explosive eruptions are driven by a more complex mix of slug and churn-annular flow that varied between and within eruptions. Discrete infrasound signals dominate during some explosive eruptions that produced significant ash plumes and PDCs, suggesting sustained fountaining (and infrasound) is not needed to produce Subplinian eruption plumes. The most energetic portion of the explosive events produced air-ground coupled waves clearly recorded on the seismometer as a shift to broader band (> 5 Hz) signals.

The seismoacoustic data from the 2023 Shishaldin eruption contain a wide variety of pre-, syn-, and post-eruptive signals. We favor a model of a foam layer of exsolved gas and magma at shallow depth that periodically collapses to produce the explosive events and associated seismoacoustic signals. Future work on these signals could focus on refining the source models and comparing them with volcanic emissions and eruption processes to better understand the dynamics and associated hazards. Additionally, although these data were useful for forecasting during the eruption sequence, future quantitative work should be performed to more robustly understand the full forecasting potential and limitations.

Supplementary information. The supplementary material contains a figure of the Events 11 and 12 infrasound and gravity waves and a figure depicting the seismic particle motion at station SSLN.

Acknowledgments. We acknowledge numerous helpful conversations on the Shishaldin eruption from members of AVO and the NSF PREEVENTS team. Jenny Nakai, Tom Parker, and Max Enders assisted with data backfilling. Laura Spina, Andrea Cannata, and Mariangela Sciotto provided helpful insight into gas flow dynamics and seismoacoustic signals at Etna. Two anonymous reviewers, Art Jolly, and the Associate Editor Ronni Grapenthin provided helpful comments that improved the manuscript.

Declarations

Funding. Funding was provided by the NSF PREEVENTS Grant 1855126 and support by the U.S. Geological Survey under Cooperative Agreement No. G24AC00240.

Conflict of interest. The authors declare no competing interests.

Data availability. Shishaldin seismoacoustic data are available through the EarthScope Consortium Web Services (https://service.iris.edu/) under network code AV (Alaska Volcano Observatory/USGS 1988).

Author contribution. DF conceptualized the project and performed the analysis with feedback from all coauthors. DT helped lead the VOISS-Net analysis and KM helped pick and quantify the infrasound metrics. DF led the writing of the manuscript. EB led the seismoacoustic network maintenance. All authors read the manuscript and provided valuable comments.

Ethics approval and consent to participate. Any use of trade, firm, or product names is for descriptive purposes only and does not imply endorsement by the U.S. Government.

Consent for publication. All authors consent to publication of this manuscript.

References

Andronico, D., Cannata, A., Di Grazia, G., Ferrari, F.: The 1986–2021 paroxysmal episodes at the summit craters of Mt. Etna: Insights into volcano dynamics and hazard. Earth-Science Reviews **220**, 103686 (2021) https://doi.org/10.1016/j.earscirev.2021.103686 .

Angarita, M., Grapenthin, R., Tan, D., Saunders-Shultz, P., Girona, T., Parameswaran, R., Lopez, T.M., Izbekov, P., Fee, D., Burgos-Delgado, V., Shreve, T., Larsen, J.: Multidisciplinary perspectives on Shishaldin Volcano: An open-system, deforming volcano. Bulletin of Volcanology (this issue)

Aki, K., Koyanagi, R.: Deep volcanic tremor and magma ascent mechanism under Kilauea, Hawaii. Journal of Geophysical Research: Solid Earth **86**(B8), 7095–7109 (1981) https://doi.org/10.1029/JB086iB08p07095 .

Alaska Volcano Observatory/USGS: Alaska Volcano Observatory. International Federation of Digital Seismograph Networks (1988). https://doi.org/10.7914/SN/AV . https://www.fdsn.org/networks/detail/AV/

Allen, R.V.: Automatic earthquake recognition and timing from single traces. Bulletin of the Seismological Society of America **68**(5) (1978)

Beyreuther, M., Barsch, R., Krischer, L., Megies, T., Behr, Y., Wassermann, J.: ObsPy: A Python Toolbox for Seismology. Seismological Research Letters **81**(3), 530–533 (2010) https://doi.org/10.1785/gssrl.81.3.530 .

Bishop, J.W., Haney, M.M., Fee, D., Matoza, R.S., McKee, K.F., Lyons, J.J.: Back-Azimuth Estimation of Air-to-Ground Coupled Infrasound from Transverse Coherence Minimization. The Seismic Record **3**(4), 249–258 (2023) https://doi.org/10.1785/0320230023 .

Bamber, E.C., La Spina, G., Arzilli, F., Polacci, M., Mancini, L., De' Michieli Vitturi, M., Andronico, D., Corsaro, R.A., Burton, M.R.: Outgassing behaviour during highly explosive basaltic eruptions. Communications Earth & Environment **5**(1), 3 (2024) https://doi.org/10.1038/s43247-023-01182-w .

Caplan-Auerbach, J., McNutt, S.R.: New insights into the 1999 eruption of Shishaldin volcano, Alaska, based on acoustic data. Bulletin of Volcanology **65**(6), 405–417 (2003) https://doi.org/10.1007/s00445-002-0267-5 .

Coppess, K., Lam, F., Dunham, E.: Volcanic eruption tremor from particle impacts and turbulence using conduit flow models. Seismica **4**(1) (2025) https://doi.org/10.26443/seismica.v4i1.1285 .

Dehn, J., Dean, K., Engle, K., Izbekov, P.: Thermal precursors in satellite images of the 1999 eruption of Shishaldin Volcano. Bulletin of Volcanology **64**(8), 525–534 (2002) https://doi.org/10.1007/s00445-002-0227-0 .

Fehler, M.: Observations of volcanic tremor at Mount St. Helens Volcano. Journal of Geophysical Research: Solid Earth **88**(B4), 3476–3484 (1983) https://doi.org/10.1029/jb088ib04p03476 . Publisher: American Geophysical Union (AGU).

Fee, D., Garces, M., Steffke, A.: Infrasound from Tungurahua Volcano 2006–2008: Strombolian to Plinian eruptive activity. Journal of Volcanology and Geothermal Research **193**(1-2), 67–81 (2010) https://doi.org/10.1016/j.jvolgeores.2010.03.006 .

Fee, D., Haney, M.M., Matoza, R.S., Van Eaton, A.R., Cervelli, P., Schneider, D.J., Iezzi, A.M.: Volcanic tremor and plume height hysteresis from Pavlof Volcano, Alaska. Science **355**(6320), 45–48 (2017) https://doi.org/10.1126/science.aah6108 .

Fee, D., Matoza, R.S.: An overview of volcano infrasound: From hawaiian to plinian, local to global. Journal of Volcanology and Geothermal Research **249**, 123–139 (2013) https://doi.org/10.1016/j.jvolgeores.2012.09.002 .

Fee, D., Tan, D., Lyons, J., Sciotto, M., Cannata, A., Hotovec-Ellis, A., Girona, T., Wech, A., Roman, D., Haney, M., De Angelis, S.: A generalized deep learning model to detect and classify volcano seismicity. Volcanica **8**(1), 305–323 (2025) https://doi.org/10.30909/vol/rjss1878 .

Girona, T., Caudron, C., Huber, C.: Origin of Shallow Volcanic Tremor: The Dynamics of Gas Pockets Trapped Beneath Thin Permeable Media. Journal of Geophysical Research: Solid Earth **124**(5), 4831–4861 (2019) https://doi.org/10.1029/2019JB017482 .

Girona, T., Fee, D., Haney, M., Power, J.A., Lopez, T.: Volcanic eruption forecasts through seismic data assimilation: The 2023 paroxysms of Shishaldin volcano, Alaska. Bulletin of Volcanology (this issue) (this issue)

Gestrich, J.E., Fee, D., Tsai, V.C., Haney, M.M., Van Eaton, A.R.: A Physical Model for Volcanic Eruption Tremor. Journal of Geophysical Research: Solid Earth **125**(10), 2019–018980 (2020) https://doi.org/10.1029/2019JB018980 .

Gomez-Patron, A., Dietterich, H., Schneider, D.: Using remote sensing to analyze pre- and co- paroxysm processes at Shishaldin volcano to improve short-term hazard forecasting. Bulletin of Volcanology (this issue) (this issue)

Haney, M., Fee, D., Lyons, J.: Waveform inversion of acoustic-gravity waves during the 2023 eruption of Shishaldin volcano, Alaska. Bulletin of Volcanology (this issue) (this issue)

Houghton, B.F., Gonnermann, H.M.: Basaltic explosive volcanism: Constraints from deposits and models. Geochemistry **68**(2), 117–140 (2008) https://doi.org/10.1016/j.chemer.2008.04.002 .

Haney, M.M., Matoza, R.S., Fee, D., Aldridge, D.F.: Seismic equivalents of volcanic jet scaling laws and multipoles in acoustics. Geophysical Journal International **213**(1), 623–636 (2018) https://doi.org/10.1093/gji/ggx554 .

Ichihara, M.: Seismic and infrasonic eruption tremors and their relation to magma discharge rate: A case study for sub-Plinian events in the 2011 eruption of Shinmoe-dake, Japan. Journal of Geophysical Research: Solid Earth **121**(10), 7101–7118 (2016) https://doi.org/10.1002/2016JB013246 .

Izbekov, P., Loewen, M., Lubbers, J., Waythomas, C.F., Wallace, K.: Petrological insights on the plumbing system of Shishaldin Volcano, Alaska: the 2023 eruption case study. Bulletin of Volcanology (this issue) (this issue)

Ichihara, M., Takeo, M., Yokoo, A., Oikawa, J., Ohminato, T.: Monitoring volcanic activity using correlation patterns between infrasound and ground motion: INFRASONIC-SEISMIC CORRELATION METHOD. Geophysical Research Letters **39**(4), (2012) https://doi.org/10.1029/2011GL050542 .

Johnson, J.B., Anderson, J., Marcillo, O., Arrowsmith, S.: Probing local wind and temperature structure using infrasound from Volcan Villarrica (Chile). Journal of Geophysical Research: Atmospheres **117**(D17), (2012) https://doi.org/10.1029/2012JD017694 .

Kim, K., Fee, D., Yokoo, A., Lees, J.M.: Acoustic source inversion to estimate volume flux from volcanic explosions. Geophysical Research Letters **42**(13), 5243–5249 (2015) https://doi.org/10.1002/2015GL064466 .

Lopez, T., Loewen, M., Lerner, A., Rasmussen, D.J., Kelly, P., Angarita, M., Wasser, V., Kushner, S., Saunders-Shultz, P., Kern, C., Werner, C., Grapenthin, R., Brewster, I., Theys, N., Franco, B., Clarisse, L.: Insights into the 2023 eruption of Shishaldin Volcano from satellite SO2 emissions and complementary datasets. Bulletin of Volcanology (this issue) (this issue)

Loewen, M.: Overview and chronology of the 2019 and 2023 eruptions of Shishaldin Volcano. Bulletin of Volcanology (this issue) (this issue)

Lyons, J.J., Tan, D., Angarita, M., Loewen, M.W., Lopez, T., Grapenthin, R., Hotovec-Ellis, A.J., Fee, D., Haney, M.M.: Identifying precursors and tracking pulses of magma ascent in multidisciplinary data during the 2018–2023 phreatomagmatic eruption at Semisopochnoi Island, Alaska. Journal of Volcanology and Geothermal Research **463**, 108329 (2025) https://doi.org/10.1016/j.jvolgeores.2025.108329 .

Longpré, M.-A., Tramontano, S., Pankhurst, M.J., Roman, D.C., Reiss, M.C., Cortese, F., James, M.R., Spina, L., Rodríguez, F., Coldwell, B., Martín-Lorenzo, A., Barbee, O., D'Auria, L., Chamberlain, K.J., Scarrow, J.H.: Shifting melt composition linked to volcanic tremor at Cumbre Vieja volcano. Nature Geoscience **18**(2), 175–183 (2025) https://doi.org/10.1038/s41561-024-01623-x .

Lyons, J.J., Waite, G.P., Rose, W.I., Chigna, G.: Patterns in open vent, strombolian behavior at Fuego volcano, Guatemala, 2005–2007. Bulletin of Volcanology **72**(1), 1–15 (2010) https://doi.org/10.1007/s00445-009-0305-7 .

Matoza, R.S., Fee, D.: Infrasonic component of volcano-seismic eruption tremor. Geophysical Research Letters **41**(6), 1964–1970 (2014) https://doi.org/10.1002/2014GL059301 .

Mota, R.: Volcanic lightning and plume dynamics during the 2023 eruption of Shishaldin Volcano, Alaska: Insights from a dry, coarse-grained, basaltic eruption. Bulletin of Volcanology (this issue) (this issue)

Nye, C., Keith, T., Eichelberger, J., Miller, T., McNutt, S., Moran, S., Schneider, D., Dehn, J., Schaefer, J.: The 1999 eruption of Shishaldin Volcano, Alaska: monitoring a distant eruption. Bulletin of Volcanology **64**(8), 507–519 (2002) https://doi.org/10.1007/s00445-002-0225-2 .

Orr, T.R., Cameron, C.E., Dietterich, H., Loewen, M., Lopez, T.M., Lyons, J.J., Nakai, J., Power, J.A., Searcy, C., Tepp, G., Waythomas, C.F.: 2020 Volcanic Activity in Alaska—Summary of Events and Response of the Alaska Volcano Observatory. Scientific Investigations Report 2024-5004 (2023). Series: Scientific Investigations Report. https://doi.org/10.3133/sir20245004

Parfitt, E.A.: A discussion of the mechanisms of explosive basaltic eruptions. Journal of Volcanology and Geothermal Research **134**(1-2), 77–107 (2004) https://doi.org/10.1016/j.jvolgeores.2004.01.002 .

Pioli, L., Bonadonna, C., Azzopardi, B.J., Phillips, J.C., Ripepe, M.: Experimental constraints on the outgassing dynamics of basaltic magmas. Journal of Geophysical Research: Solid Earth **117**(B3), 2011–008392 (2012) https://doi.org/10.1029/2011JB008392 .

Pioli, L., Erlund, E., Johnson, E., Cashman, K., Wallace, P., Rosi, M., Delgado Granados, H.: Explosive dynamics of violent Strombolian eruptions: The eruption of Parícutin Volcano 1943–1952 (Mexico). Earth and Planetary Science Letters **271**(1-4), 359–368 (2008) https://doi.org/10.1016/j.epsl.2008.04.026 .

Petersen, T., McNutt, S.R.: Seismo-acoustic signals associated with degassing explosions recorded at Shishaldin Volcano, Alaska, 2003–2004. Bulletin of Volcanology **69**(5), 527–536 (2007) https://doi.org/10.1007/s00445-006-0088-z .

Ripepe, M., Barfucci, G., De Angelis, S., Delle Donne, D., Lacanna, G., Marchetti, E.: Modeling Volcanic Eruption Parameters by Near-Source Internal Gravity Waves. Scientific Reports **6**(1), 36727 (2016) https://doi.org/10.1038/srep36727 .

Ripepe, M., Marchetti, E., Delle Donne, D., Genco, R., Innocenti, L., Lacanna, G., Valade, S.: Infrasonic Early Warning System for Explosive Eruptions. Journal of Geophysical Research: Solid Earth **123**(11), 9570–9585 (2018) https://doi.org/10.1029/2018JB015561 .

Rasmussen, D.J., Plank, T.A., Roman, D.C., Power, J.A., Bodnar, R.J., Hauri, E.H.: When does eruption run-up begin? Multidisciplinary insight from the 1999 eruption of Shishaldin volcano. Earth and Planetary Science Letters **486**, 1–14 (2018) https://doi.org/10.1016/j.epsl.2018.01.001 .

Romero, J.E., Vera, F., Polacci, M., Morgavi, D., Arzilli, F., Alam, M.A., Bustillos, J.E., Guevara, A., Johnson, J.B., Palma, J.L., Burton, M., Cuenca, E., Keller, W.: Tephra From the 3 March 2015 Sustained Column Related to Explosive Lava Fountain Activity at Volcán Villarrica (Chile). Frontiers in Earth Science **6**, 98 (2018) https://doi.org/10.3389/feart.2018.00098 .

Stelling, P., Beget, J., Nye, C., Gardner, J., Devine, J., George, R.: Geology and petrology of ejecta from the 1999 eruption of Shishaldin Volcano, Alaska. Bulletin of Volcanology **64**(8), 548–561 (2002) https://doi.org/10.1007/s00445-002-0229-y . Publisher: Springer Science and Business Media LLC.

Spina, L., Cannata, A., Morgavi, D., Perugini, D.: Degassing behaviour at basaltic volcanoes: New insights from experimental investigations of different conduit geometry and magma viscosity. Earth-Science Reviews **192**, 317–336 (2019) https://doi.org/10.1016/j.earscirev.2019.03.010 .

Sciotto, M., Cannata, A., Prestifilippo, M., Scollo, S., Fee, D., Privitera, E.: Unravelling the links between seismo-acoustic signals and eruptive parameters: Etna lava fountain case study. Scientific Reports **9**(1), 16417 (2019) https://doi.org/10.1038/

s41598-019-52576-w .

Seyfried, R., Freundt, A.: Experiments on conduit flow and eruption behavior of basaltic volcanic eruptions. Journal of Geophysical Research: Solid Earth **105**(B10), 23727–23740 (2000) https://doi.org/10.1029/2000JB900096 .

Szramek, L.A.: Mafic Plinian eruptions: Is fast ascent required? Journal of Geophysical Research: Solid Earth **121**(10), 7119–7136 (2016) https://doi.org/10.1002/2016JB013208 .

Tan, D., Fee, D., Witsil, A., Girona, T., Haney, M., Wech, A., Waythomas, C., Lopez, T.: Detection and Characterization of Seismic and Acoustic Signals at Pavlof Volcano, Alaska, Using Deep Learning. Journal of Geophysical Research: Solid Earth **129**(6), 2024–029194 (2024) https://doi.org/10.1029/2024JB029194 .

Thompson, G., McNutt, S., Tytgat, G.: Three distinct regimes of volcanic tremor associated with the eruption of Shishaldin Volcano, Alaska 1999. Bulletin of Volcanology **64**(8), 535–547 (2002) https://doi.org/10.1007/s00445-002-0228-z .

Ulivieri, G., Ripepe, M., Marchetti, E.: Infrasound reveals transition to oscillatory discharge regime during lava fountaining: Implication for early warning. Geophysical Research Letters **40**(12), 3008–3013 (2013) https://doi.org/10.1002/grl.50592 .

Vergniolle, S., Boichu, M., Caplan-Auerbach, J.: Acoustic measurements of the 1999 basaltic eruption of Shishaldin volcano, Alaska. Journal of Volcanology and Geothermal Research **137**(1-3), 109–134 (2004) https://doi.org/10.1016/j.jvolgeores.2004.05.003 .

Vergniolle, S., Caplan-Auerbach, J.: Basaltic thermals and Subplinian plumes: Constraints from acoustic measurements at Shishaldin volcano, Alaska. Bulletin of Volcanology **68**(7-8), 611–630 (2006) https://doi.org/10.1007/s00445-005-0035-4 .

Vergniolle, S.: Origin of Basaltic Subplinian Eruption at Shishaldin Volcano (Alaska): A Vigorously Degassing Magma Reservoir Hosting Small Bubbles. Journal of Geophysical Research: Solid Earth **129**(8) (2024) https://doi.org/10.1029/2023jb028161 . Publisher: American Geophysical Union (AGU).

Vergniolle, S., Jaupart, C.: Separated two-phase flow and basaltic eruptions. Journal of Geophysical Research: Solid Earth **91**(B12), 12842–12860 (1986) https://doi.org/10.1029/JB091iB12p12842 .

Vergniolle, S., Ripepe, M.: From Strombolian explosions to fire fountains at Etna Volcano (Italy): What do we learn from acoustic measurements? Geol. Soc. Spec. Publ. **307**, 103–124 (2008) https://doi.org/10.1144/SP307.7

Waythomas, C.F.: Emplacement of Volcaniclastic Mass Flows during the 2023 Eruption of Shishaldin Volcano, Alaska. Bulletin of Volcanology (this issue) (this

issue)

Wilson, L.: Relationships between pressure, volatile content and ejecta velocity in three types of volcanic explosion. Journal of Volcanology and Geothermal Research **8**(2-4), 297–313 (1980) https://doi.org/10.1016/0377-0273(80)90110-9

Supplemental Information for

Seismic and infrasound signals from the 2023 explosive eruption sequence of Shishaldin Volcano, Alaska

David Fee[1*], Darren Tan[1], Matthew Haney[2], Karenna Merritt[1], John Lyons[2], Aaron Wech[2], Matthew Loewen[2], Eleanor Boyce[1], Logan Scamfer[1]

[1*]Alaska Volcano Observatory, Geophysical Institute, University of Alaska Fairbanks, 2156 Koyukuk Dr, Fairbanks, 99775, AK, USA.
[2]Alaska Volcano Observatory, U.S. Geological Survey, 4230 University Drive, Anchorage, 999508, AK, USA.

*Corresponding author(s). E-mail(s): dfee1@alaska.edu;
Contributing authors: ptan@alaska.edu; mhaney@usgs.gov; kamerritt@alaska.edu; jlyons@usgs.gov; awech@usgs.gov; mloewen@usgs.gov; esboyce@alaska.edu; ltscamfer@alaska.edu;

1 Supplemental Information

1.1 Gravity Waves for Events 11 and 12

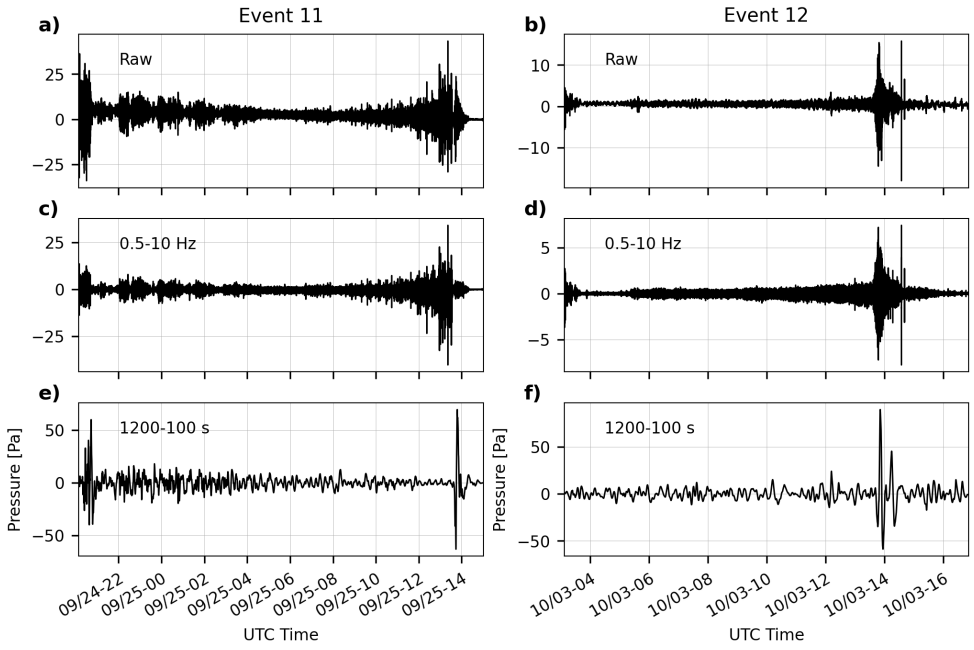

Fig. S1 Comparison of the infrasound and gravity wave observations for Events 11 and 12. The data from SSLS infrasound are unfiltered (a,b), filtered between 0.5–10 Hz (c,d), and filtered between 1200–100 s for Events 11 (left panels) and 12 (right panels). Data are shown for the identified infrasound signal duration plus 30 min before and after. The 1200–100 s band highlights the energetic gravity wave towards the end of each eruption, and the full frequency response has been removed using a cosine-tapered bandpass filter between 10,000 s and the Nyquist frequency.

1.2 Acoustic-Seismic Coupling Particle Motion and TCM

As described in the main text, we select the prograde particle motion solution within the TCM algorithm (Bishop et al. 2023) when estimating the back-azimuth of air-to-ground coupled infrasound at SSLN. Selecting the prograde solution slightly departs from the original algorithm, which resolves a 180° ambiguity by assuming retrograde particle motion. While retrograde motion in acoustic-seismic coupling is commonly assumed, prograde particle motion can exist when subsurface shear-wave velocities are particularly low (Bishop et al. 2022; Langston 2004).

We justify the prograde solution through the analysis of the seismic particle motion. We utilize the Normalized Inner-Product (NIP) method (Meza-Fajardo et al. 2015)

to examine the frequency-dependent phase between radial and vertical seismic displacements. To compute the NIP, we rotate seismograms toward Shishaldin's summit crater. Figure S2 examines the sense of particle motion at SSLN between 1–20 Hz for the same time window shown in Figure 7 of the main text. We see that above ≈12 Hz in panel d), prograde motion dominates. Since this is also the region with the highest seismoacoustic coherence, the selection of a prograde TCM solution is required for an accurate TCM estimate. The particle motion also has a clear frequency dependence, likely caused by variations in subsurface structure. Higher frequencies sample shallower depths, where materials with sufficiently low shear-wave velocities allow prograde motion to occur.

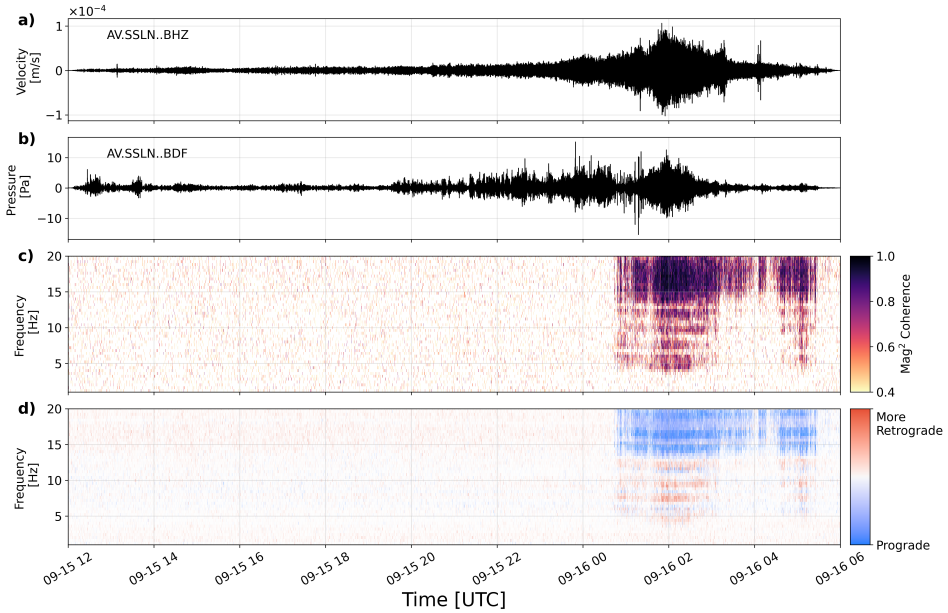

Fig. S2 Air-to-ground coupled wave particle motion for Event 10 on September 15, 2023 at SSLN. The time window examined here is the same as Figure 7 in the main text. a) Seismic and b) infrasound waveforms filtered between 1–20 Hz c) Coherence between the infrasound and vertical seismic. d) Particle motion analysis showing the NIP value, where blue (-1) indicates prograde particle motion, and red (+1) indicates retrograde particle motion. The transparency of this panel is determined by the magnitude-squared coherence above, to better focus on particle motions associated with seismoacoustic coupling

References

Bishop, J.W., Fee, D., Modrak, R., Tape, C., Kim, K.: Spectral Element Modeling of Acoustic to Seismic Coupling Over Topography. Journal of Geophysical Research: Solid Earth **127**(1), 2021–023142 (2022) https://doi.org/10.1029/2021JB023142 . _eprint: https://onlinelibrary.wiley.com/doi/pdf/10.1029/2021JB023142

Bishop, J.W., Haney, M.M., Fee, D., Matoza, R.S., McKee, K.F., Lyons, J.J.: Back-Azimuth Estimation of Air-to-Ground Coupled Infrasound from Transverse Coherence Minimization. The Seismic Record **3**(4), 249–258 (2023) https://doi.org/10.1785/0320230023

Langston, C.A.: Seismic ground motions from a bolide shock wave. Journal of Geophysical Research: Solid Earth **109**(B12) (2004) https://doi.org/10.1029/2004JB003167 . _eprint: https://onlinelibrary.wiley.com/doi/pdf/10.1029/2004JB003167

Meza-Fajardo, K.C., Papageorgiou, A.S., Semblat, J.: Identification and Extraction of Surface Waves from Three-Component Seismograms Based on the Normalized Inner Product. Bulletin of the Seismological Society of America **105**(1), 210–229 (2015) https://doi.org/10.1785/0120140012